

A Deep *Chandra* ACIS Study of NGC 4151. III. the Line Emission and Spectral Analysis of the Ionization Cone

Junfeng Wang¹, Giuseppina Fabbiano¹, Martin Elvis¹, Guido Risaliti^{1,2}, Margarita Karovska¹, Andreas Zezas^{1,3}, Carole G. Mundell⁴, Gaelle Dumas⁵, and Eva Schinnerer⁵

juwang@cfa.harvard.edu

ABSTRACT

This paper is the third in a series in which we present deep *Chandra* ACIS-S imaging spectroscopy of the Seyfert 1 galaxy NGC 4151, devoted to study its complex circum-nuclear X-ray emission. Emission features in the soft X-ray spectrum of the bright extended emission ($L_{0.3-2\text{keV}} \sim 10^{40} \text{ erg s}^{-1}$) at $r > 130 \text{ pc}$ ($2''$) are consistent with blended brighter OVII, OVIII, and NeIX lines seen in the *Chandra* HETGS and XMM-Newton RGS spectra below 2 keV. We construct emission line images of these features and find good morphological correlations with the narrow line region clouds mapped in [OIII] $\lambda 5007\text{\AA}$. Self-consistent photoionization models provide good descriptions of the spectra of the large scale emission, as well as resolved structures, supporting the dominant role of nuclear photoionization, although displacement of optical and X-ray features implies a more complex medium. Collisionally ionized emission is estimated to be $\lesssim 12\%$ of the extended emission. Presence of both low and high ionization spectral components and extended emission in the X-ray image perpendicular to the bicone indicates leakage of nuclear ionization, likely filtered through warm absorbers, instead of being blocked by a continuous obscuring torus. The ratios of [OIII]/soft X-ray flux are approximately constant (~ 15) for the 1.5 kpc radius spanned by these measurements, indicating similar relative contributions from

¹Harvard-Smithsonian Center for Astrophysics, 60 Garden St, Cambridge, MA 02138

²INAF-Arcetri Observatory, Largo E, Fermi 5, I-50125 Firenze, Italy

³Physics Department, University of Crete, P.O. Box 2208, GR-710 03, Heraklion, Crete, Greece

⁴Astrophysics Research Institute, Liverpool John Moores University, Birkenhead CH41 1LD, UK

⁵Max-Planck-Institut für Astronomie, Königstuhl 17, D-69117 Heidelberg, Germany

the low- and high-ionization gas phases at different radial distances from the nucleus. If the [OIII] and X-ray emission arise from a single photoionized medium, this further implies an outflow with a wind-like density profile. Using spatially resolved X-ray features, we estimate that the mass outflow rate in NGC 4151 is $\sim 2M_{\odot} \text{ yr}^{-1}$ at 130 pc and the kinematic power of the ionized outflow is $1.7 \times 10^{41} \text{ erg s}^{-1}$, approximately 0.3% of the bolometric luminosity of the active nucleus in NGC 4151.

Subject headings: X-rays: galaxies — galaxies: Seyfert — galaxies: jets — galaxies: individual (NGC 4151)

1. Introduction

The Seyfert 1 galaxy NGC 4151 is well known to have an extended narrow line region (ENLR) in the optical (e.g., Perez et al. 1989; Robinson et al. 1994; Crenshaw et al. 2000), indicating interaction between the active galactic nucleus (AGN) and the host galaxy (Unger et al. 1987). Thanks to its proximity ($d \sim 13.3 \text{ Mpc}$, $1'' = 65 \text{ pc}$; Mundell et al. 1999) and extensive coverage at all wavelengths (Ulrich 2000 and references therein), NGC 4151 thus represents an excellent laboratory to study observationally nuclear feedback.

Presence of extended emission in the soft X-rays is also well established (Elvis et al. 1983; Morse et al. 1995; Ogle et al. 2000; Yang et al. 2001; Wang et al. 2010a, 2011a). The nature of the kpc-scale extended X-ray emission remains uncertain; suggestions include collisionally ionized plasma, photoionized gas, a hybrid of both, or electron-scattered nuclear emission (Elvis et al. 1983, 1990; Heckman & Balick 1983; Morse et al. 1995; Schulz & Komossa 1993; Ogle et al. 2000; Komossa 2001; Yang et al. 2001), although electron-scattering is less favored, because the required scattering column and spectral variability do not match the observations (Weaver et al. 1994; Yang et al. 2001). Previous *Chandra* imaging studies of NGC 4151 (Ogle et al. 2000; Yang et al. 2001; Gonzalez Martin 2008; Wang et al. 2009, 2010a) found good morphological agreements between the extended X-ray emission and the optical forbidden line emission (in particular [OIII] $\lambda 5007$). Such a close spatial correspondence between the soft X-rays and the [OIII] emission appears to be common in nearby Seyfert 2 galaxies, leading Bianchi et al. (2006) to propose that optical and X-ray features arise from a single photoionized medium.

High spectral resolution grating observations of NGC 4151 with *Chandra* and *XMM-Newton* further show that the soft X-ray emission is due to both blended emission lines and radiative recombination continua (RRC) from He-like and H-like transitions of carbon,

oxygen, neon, and nitrogen (Ogle et al. 2000; Schurch et al. 2004; Armentrout et al. 2007). The X-ray line ratio diagnostics and electron temperatures of the RRC features support the conclusion that most of the gas is photoionized ($T \sim 10^4$ K) by the AGN (Schurch et al. 2004; Armentrout et al. 2007), although photoexcitation by the AGN continuum may also play an important role (Kinkhabwalla et al. 2003, Ogle et al. 2003).

However, these grating studies of NGC 4151 cannot provide the spatial distribution of each spectral feature. The extracted spectra consist of both nuclear emission and extended emission from various physical scales. Therefore, based on the high resolution spectra alone, one cannot exclude that the photoionized emission may be associated with the bright narrow-line region (NLR) gas clouds close to the nucleus ($\ll 100$ pc), while a significant contribution from collisionally ionized gas may be present at larger radii (e.g., NGC 1365, Wang et al. 2009, Guainazzi et al. 2009). Although Yang et al. (2001) presented ACIS imaging data, the limited signal to noise ratio (S/N) of these data prevented detailed high spatial resolution comparisons of optical [OIII] and X-ray morphology, or the spectral analysis of X-ray emission from the spatially resolved features.

The X-ray emission mechanisms in this prototypical Seyfert 1 galaxy deserve further investigation with high quality X-ray data that allow spatially resolved spectral analysis of the circum-nuclear region. This is the aim of the study presented in this paper, the sixth and last in our series of studies on the nuclear and circum-nuclear region of NGC 4151 using deep *Chandra* ACIS and HRC observations (PI: Fabbiano). Using the HRC data and image deconvolution techniques, Wang et al. (2009) resolved the nuclear emission on spatial scale of ~ 30 pc and made comparisons with *HST* observations. Wang et al. (2010a) presented the X-ray spectral analysis of the NGC 4151 nuclear emission. Wang et al. (2010b) reported the discovery of faint soft X-ray emission extending 2 kpc out from the active nucleus and filling in the cavity of the H I material. In Paper I of the present series (Wang et al. 2011a), based on in-depth analysis of the ACIS data set, we have examined the kpc scale X-ray morphology and the relations between X-ray absorption features and the cold ISM in the host galaxy. In Paper II (Wang et al. 2011b) we have reported on strong evidence of jet–cloud interaction in the nuclear region ($r \leq 130$ pc) and compared these findings to our previous HRC study. Here we focus on the comparison between the X-ray line emission of the ionization cone and the ionized gas traced by the optical line emission, and we report on the spectral analysis of spatially resolved X-ray features. The paper is organized as follows. In § 2, we first briefly describe the data reduction, present the X-ray emission line morphologies (§ 2.1) and the spectral modeling of all extended emission within a $30''$ -radius (~ 2 kpc) and the spatially resolved emission (§ 2.2). The results are discussed in § 3 and summarized in § 4.

2. Data Extraction and Analysis

NGC 4151 was observed by *Chandra* for a total of 180 ks (after screening for high background intervals) with the spectroscopic array of the Advanced CCD Imaging Spectrometer (ACIS-S; Garmire et al. 2003) in 1/8 sub-array mode during March 27-29, 2008. We have presented the details of our ACIS observations of NGC 4151 and the data reduction in Paper I.

The data were analyzed following the standard procedures using CIAO (Version 4.2) with the CALDB 4.2.1 provided by the *Chandra* X-ray Center (CXC). Subpixel event repositioning and subpixel binning techniques (Paper I and references therein) have been applied to the ACIS images to improve the spatial resolution.

The complexity in the data analysis caused by the bright nuclear emission was described in Papers I and II. We established that for the *soft* X-ray emission ($E < 1$ keV), photon pile-up is most severe in the inner $r < 1''$, mild at $1'' \lesssim r \lesssim 2''$, and not an issue at $r > 2''$. *Chandra* PSF simulations were performed to provide an estimate of the expected contamination from the nuclear emission in an extended feature. We have taken into account this information in the following analysis.

2.1. Broad-band Images and X-ray Emission Line Maps

Figure 1 (top) shows the 0.3–2 keV ACIS image ($\sim 0.5''$ per pixel). Bright structured soft X-ray emission along the northeast (NE) – southwest (SW) direction is apparent, together with fainter, less extended emission along the northwest (NW) – southeast (SE) direction. The inner $r < 2''$ nuclear region, where we identified interactions between the radio jet and the optical clouds, has been discussed in Paper II. Here we focus on the kpc-scale extended emission. We first extracted counts from every 10° sectors to create azimuthal surface brightness profiles for the extended X-ray emission ($2'' \leq r \leq 30''$), which provides a clear view of its angular distribution, and to identify sectors that contain the bright outflows (Figure 1, bottom). This plot was used to guide further spectral extraction (see § 2.2.2). The extended emission along the NW–SE direction is interesting as this is the direction of the putative obscuring torus. Figure 2 demonstrates the clear elongation perpendicular to the bicone (in particular the NW sector), using the 0.3–2 keV ACIS image smoothed with the CIAO tool *csmooth*. We extracted the 0.3–2 keV radial profiles of the NW sector, the bright SW cone, and the faint emission in between (the “control region”), shown in Figure 3. The NW emission is on average 5 times fainter than the bright SW cone, but brighter than the control region at $r < 7''$ (4σ significance). Beyond $r = 7''$, it becomes indistinguishable

with the faint emission. The implication on the nuclear obscuring structure will be discussed later in § 3.2.

A quick examination of the spectrum of the extended emission extracted from a circular region between a radius of $2''$ and $30''$ shows the clear presence of strong blended emission lines (Figure 4), corresponding to the emission lines (<2 keV) seen in HETG observations (Ogle et al. 2000). These lines cannot be uniquely resolved with the spectral resolution of the ACIS imaging observation. Most notably the blended lines appear as three strong emission features approximately centered at 0.57 keV (OVII), 0.68 keV (OVIII), 0.91 keV (NeIX) and a few weak lines between 1–2 keV (Mg XI, Si $K\alpha$, SiXIII; Figure 4). The blended emission features seen in the ACIS spectrum and the corresponding HETG lines are summarized in Table 1 (see § 2.2.1).

Following Paper II, we created adaptively smoothed images of the NGC 4151 circum-nuclear region using the subpixel resolution data. We extracted images from the merged data in three spectral bands dominated by emission lines below 2 keV: 0.3–0.7 keV (“soft band” containing the OVII and OVIII emission), 0.7–1.0 keV (“medium band” containing the NeIX emission), and 1–2 keV (“hard band”). Figure 5a presents a false color composite image of the central $\sim 45'' \times 45''$ (~ 3 kpc on a side), circum-nuclear region of NGC 4151, where the soft, medium, and hard band smoothed images are shown in red, green, and blue, respectively. Figure 5b zooms in to the central 1 kpc-radius region, emphasizing the bicone emission. For visualization of the faint features, the nuclear region (see Paper II) is saturated and excluded from this figure. The X-ray biconical morphology has been described in Paper I, and here we focus on the spectral differences. The extended bicone emission ($> 2''$) appears rich in 0.3–1 keV emission (red and green). Similar color emission (mixed red/green) is also seen perpendicular to the bicone direction with a hint of harder (blue) emission. Clumps of 0.3–0.7 keV (red; OVII and OVIII) emission are also seen, some particularly prominent features are seen in the SW cone $\sim 6''$ and $\sim 10''$ from the nucleus.

To further highlight the regions where the strong emission lines arise, we also extracted the X-ray emission in narrow energy intervals (0.53–0.63 keV; 0.63–0.73 keV; 0.85–0.95 keV) to create line strength images. This is a reasonable approach since the line emission dominates over the weak underlying continuum (Schurch et al. 2004) in these narrow bands. The resulting images are shown in Figure 6. The position of the nucleus is indicated with a black cross. OVII and OVIII line emission is prevalent in the extended regions. NeIX emission, while extended along the general P.A. of the large scale extended emission, is bright in the central $r = 2''$ but becomes fainter quickly at $r \gtrsim 3''$ compared to the OVII emission. We examined similar emission line maps for the weak lines in the 1–2 keV range (NeX, NeIX RRC, MgXI) and found that they are highly concentrated within the inner $r = 2''$ region.

This is better demonstrated in Figure 6d, where the radial profiles of the line emissions are shown.

2.2. Spectral Analysis

Spectra and instrument responses were generated using CIAO Version 4.2 and analyzed with XSPEC Version 12.6 (Arnaud 1996). Background spectra were taken from a source-free region from the same chip. Spectra were grouped to have at least 20 counts per energy bin to allow χ^2 fitting. Unless otherwise noted, we restricted our modeling to photon energies above 0.3 keV, where the ACIS calibration is good¹, and below 2 keV, above which the nuclear continuum dominates (Wang et al. 2010b). The 90% confidence interval for a single interesting parameter is reported for all fitting results.

2.2.1. The 30''-radius Extended Emission as a Testbed

We first characterize the X-ray spectrum of bright extended emission extracted from the $2'' \leq r \leq 30''$ circular region, exploring a phenomenological spectral fitting approach that was broadly adopted in previous studies at CCD resolution (Yang et al. 2001; see also Ogle et al. 2000, Smith & Wilson 2001). The “continuum” in the ACIS spectrum (a combination of true underlying continuum and highly blended weak emission lines) was described by a smooth bremsstrahlung emission. We emphasize that the bremsstrahlung emission here should not be assigned any physical origin, whereas the derived line emission should be considered as a lower limit in such an approach.

Repeating the technique used to fit the spectrum of the nucleus (Wang et al. 2010), narrow emission lines were then added to the model. The *Chandra* HETG and *XMM-Newton* RGS spectra (Ogle et al. 2000; Schurch et al. 2004; Armentrout et al. 2007) were used as a guide for the identification of the soft X-ray lines. The X-ray spectrum of the nucleus of NGC 4151 is notoriously complex and variable. The hard X-ray continuum is dominated by a power law component suppressed by a partially covering absorber and a Compton reflection component (Weaver et al. 1994; Schurch et al. 2004; De Rosa et al. 2007; Wang et al. 2010b; Lubinski et al. 2010), and the absorption consists of both a mildly-ionized “warm absorber” and a cold absorber (Kraemer et al. 2005; González-Martín 2008). The PSF scattered contribution from the nuclear emission is taken into account in the spectral fitting,

¹See <http://cxc.cfa.harvard.edu/cal/Acis/>

using the nuclear component fixed at the best fit nuclear spectral model and normalization (Wang et al. 2010b) scaled to the expected fraction from PSF simulations. The extraction region contains 4.7% of the 0.3–2 keV nuclear emission due to PSF scattering, corresponding to $\sim 25\%$ of the extracted counts. This can be taken as the upper limit of contamination to the extended line emission, as the line emission dominates the nuclear spectrum.

The identified emission line blends are summarized in Table 1 and the spectrum shown in Figure 7 (see also Figure 4). The absorption column required by the fit is consistent with the line-of-sight Galactic column towards NGC 4151 ($N_H = 2.1 \times 10^{20} \text{ cm}^{-2}$; Murphy et al. 1993). The X-ray luminosity of the extended emission (between 130 pc and 2 kpc from the nucleus) corrected for the Galactic absorption is $L_{0.3-2\text{keV}} = 1.1 \pm 0.2 \times 10^{40} \text{ erg s}^{-1}$, compared with $L_{2-10\text{keV}} = 2 \times 10^{42} \text{ erg s}^{-1}$ for the unabsorbed nuclear source (Wang et al. 2010b).

However, such a simplified model does not provide constraints on the emission mechanism, and more physically meaningful spectral models are needed. Fitting the data with combinations of absorbed optically-thin thermal emission with solar abundances (*APEC* model; Smith et al. 2001) was attempted but gave poor results (reduced $\chi^2_\nu > 3$). The abundances were then allowed to vary from solar abundance in the *APEC* model using the variable abundance *APEC* model (*VAPEC*), in which Z_O , Z_{Ne} , Z_{Si} , and Z_{Fe} were left free while other elements were fixed at solar abundance. When Z is allowed to vary, the fit generally improves but still is far from satisfactory ($\chi^2_\nu \sim 2$). Moreover, the required abundances become unphysically low ($Z < 0.01Z_\odot$) as the fit attempts to reproduce a smooth continuum.

To have a self-consistent model, we have made use of the *Cloudy* photoionization modeling code (Ferland et al. 1998). Although the resolution of the ACIS CCD spectrum prevents us from performing line-based diagnostics, e.g. deriving line ratios of the Helium-like triplets, spectral fitting with photoionization models still provides useful constraints about the photoionization status (as in Bianchi et al. 2006, 2010; Gonzalez-Martin et al. 2010). Using *Cloudy* version C08.00, which enables a *Cloudy*/XSPEC interface (Porter et al. 2006), we modelled the $< 2 \text{ keV}$ X-ray spectrum assuming an open plane-parallel geometry (“slab”). The dimensionless ionization parameter (Osterbrock & Ferland 2006) is defined as $U = Q/(4\pi r^2 c n_H)$, where n_H is the hydrogen number density, r is the distance to the inner face of a model slab, c is the speed of light, and $Q = \int_{13.6\text{eV}}^\infty L_\nu/h\nu$ is the emitting rate of hydrogen ionizing photons (s^{-1}) by the ionizing source. We assumed the broken power-law used by Kraemer et al. (2005) for the AGN continuum (see also Armentrout et al. 2007). We varied U and N_H , the column density of the slab to create spectral models covering a grid of parameters ($-3 \leq \log U \leq 3$, $19.0 \leq \log N_H \leq 23.5 \text{ cm}^{-2}$), which were fed to XSPEC.

Armentrout et al. (2007) successfully modeled the XMM-Newton/RGS soft X-ray spectrum of NGC 4151 with three photoionization components: a high ionization component ($\log U = 1.3$, $\log N_H = 23.0$), a medium ionization component ($\log U = 0$, $\log N_H = 23.0$), and a low ionization component ($\log U = -0.5$, $\log N_H = 20.5$). In our initial attempt, we included all these components, with the ionization parameters and the column densities fixed at these values and the normalizations set free. In addition, the photoionized emission was absorbed with a line-of-sight column density, $N_{H,l.o.s.}$. The fit to the ACIS spectrum was poor ($\chi^2_\nu \geq 6$). This is not a total surprise, given that these best fit parameters, are optimized for the brightest photoionized material close to the nucleus (10^{-3} –1 pc; Armentrout et al. 2007) that dominates the soft X-ray spectrum of NGC 4151, whereas the emission of interest here arise on the $r \sim 130$ pc–1.5 kpc scale.

When the (U , N_H) parameters for the photoionized components were set free to vary, we were able to obtain a statistically satisfactory fit ($\chi^2_\nu = 1.1$), reproducing the observed ACIS spectrum of the large scale extended X-ray emission well (Figure 8). The line-of-sight column density required by the fit is $N_{H,l.o.s.} = 2 \times 10^{20} \text{ cm}^{-2}$, consistent with the Galactic column towards NGC 4151 (Murphy et al. 1996). Two components, a high ionization phase ($\log U = 0.8$, $\log N_H = 20.0$) and a low ionization phase ($\log U = -0.25$, $\log N_H = 19.4$), are required to produce both the hydrogen-like and helium-like neon and oxygen line emissions. The *Cloudy* model predicts gas pressures of $6 \times 10^{-7} \text{ dynes cm}^{-2}$ and $1.3 \times 10^{-7} \text{ dynes cm}^{-2}$ for the high U component and low U component, respectively. If they are collocated, additional pressure—perhaps from a hot intercloud medium in a multiphase ISM (Elvis et al. 1983, Ogle et al. 2000)—is needed to reach pressure equilibrium. Note that the $\log U = -0.25$ component closely resembles the “Low” model component in Armentrout et al. (2007) and the “D+Ea” X-ray absorption component in Kraemer et al. (2005).

These model components still left small residuals at ~ 0.5 keV (the NVII Ly α) and 1.02 keV (the NeX Ly α). Adding in a third photoionized component can further improve the fit (best fit parameters $\log U = 1.23$, $\log N_H = 19.2$), but the improvement appears not significant when an F -test is performed (at 70% significance level). Thus the two-component model is used as a template for the following analysis of subregions.

Given the satisfactory spectral fits with photoionized components and lack of clear signatures of collisional ionization in the ENLR, how much thermal emission from hot gas may be present in the circum-nuclear region of NGC 4151? We obtain a constraint on the possible presence of the hot ISM by invoking a collisionally ionized component in the best fit photoionization model. After adding a thermal emission component (*APEC*) to the photoionized emission, the fit is improved with a $kT = 0.81 \pm 0.05$ keV (at $> 99\%$ significant level by F -test) and the residual at 0.9–1.1 keV is mostly accounted for. This thermal

component may contribute $\lesssim 12\%$ of the total soft X-ray emission, $L_{th,0.5-2\text{keV}} = 6 \times 10^{38}$ erg s $^{-1}$. As a cautionary note, although *APEC* component improves the fit statistically, it remains possible that the residuals are due to photoexcitation of Fe L-shell and the enhanced resonance lines (e.g., Ogle et al. 2003; Kinkhabwala et al. 2003) that are inadequately accounted for with the *Cloudy* photoionization model components. This will be explored with the high resolution HETG spectrum in future work. We will discuss the possible presence of the thermal component further.

We emphasize that, because of likely complex geometrical dependencies and absorption between these components in the kpc scale emission, this modeling may still be over-simplistic to simultaneously reproduce the observed features in the broad band.

2.2.2. Spectral Fitting of Selected Subregions

To perform spectral analysis of the extended X-ray emission, the large scale region was divided into four sectors with position angles (P.A.) as outlined in Figure 1. Extraction regions are termed the “SW”, “NW”, “SE” and “NE” regions respectively (Table 2; see Figure 1). The bisectors of NE and SW correspond to the approximate P.A. of the ENLRs (e.g., Robinson et al. 1994). They are further divided into subregions along the radial direction (e.g., SW 1, 2, 3, and 4; NE 1, 2, and 3), with ~ 1000 counts (0.3–2 keV) in the fainter outer regions (SW4 and NE3). The NW and SE sectors cover regions ($2'' \leq r \leq 15''$) perpendicular to the bicone, which is the direction of the large scale weak bar (Asif et al. 1998).

Corresponding to the variations in color, spectral differences are clearly visible when the ACIS spectra across sectors are compared (Figure 9). The fitting results are summarized in Table 2, and Figures 10, 11, and 12 show the corresponding spectra and the fits. We find that:

1. Except for the outer-most regions (NE3 and SW4), a high ionization component is present in all regions ($\log U \sim 0.83\text{--}1.26$). Lower ionization components are present along the bicone direction (NE–SW), with $\log U$ values ranging between -0.5 and 0 . Recall that the fit to the integrated spectrum, which includes emission from all the subregions, finds the $\log U \sim 0.8$ and $\log U \sim -0.25$ components.
2. In the NE3 and SW4 regions, a very low ionization component ($\log U > -1$) and a high column density ($\log N_H = 23.5$) are required by the fit to improve the residuals in the MgI $K\alpha$ and SiI $K\alpha$. An F-test indicates that this fluorescent component significantly improve the fit at 98% confidence.

3. The second photoionized component in the NW–SE regions, perpendicular to the ionization cone, shows a lower ionization ($\log U \sim -1$).

We also extracted spectra of the X-ray emission in the bicone regions that are prominent in 0.3–0.7 keV emission (or “OVII” rich, visually red in Figure 5) and in 0.7–1 keV emission (or “NeIX” rich, visually green in Figure 5). The spectral fits are shown in Figure 13a,b respectively. Whereas the fitted ionization parameter for the “NeIX” rich emission is close to the average value, the “OVII” rich emission is generally of lower ionization, likely due to higher number density. This is consistent with the appearance of clumpy material in the optical.

3. Discussion

3.1. Nature of ENLR Emission: Photoionization and Collisional Ionization

Kiloparsec-scale extended X-ray emission is ubiquitously observed in nearby obscured Seyfert galaxies with ENLRs (Bianchi et al. 2006; Guainazzi et al. 2009; Bianchi et al. 2010; Gonzalez-Martin et al. 2010), but the ionization mechanism for this emission has been a subject of active debate. For NGC 4151, Yang et al. (2001) proposed a two phase model for the extended X-ray emission, including a photoionized warm gas and a hotter collisionally ionized gas (see also Komossa 2001). The relatively low electron temperatures ($T \sim 10^4 - 10^5$ K) inferred from the radiative recombination continua (RRC; see Liedahl 1999 for review) and the line ratios from the He-like triplets strongly support the presence of a photoionized component (Ogle et al. 2000; Schurch et al. 2004; Kraemer et al. 2005). However, does the observed soft spectrum entirely consist of photoionized emission, or does collisional ionization become more important than the photoionization mechanism beyond the nuclear region (Armentrout et al. 2007)?

3.1.1. *Evidences for Photoionization as the Dominant Ionization Mechanism*

Several of our results point to photoionization as the dominant mechanism.

- *Emission Line Gas Morphologies* — First of all, the morphological agreement between soft X-ray and optical [OIII] emission is very strong. In particular, there is a good spatial correlation between [OIII] line emission and the three strong X-ray emission lines (Figures 6a-c). There is clearly an overall morphological coincidence with the

ionized gas bicone traced by [OIII] emission, as noted in previous X-ray studies (e.g., Ogle et al. 2000, Yang et al. 2001). A good agreement between the peaks of optical and X-ray line emissions in the inner $r = 3''$ is found.

- *[OIII]-to-Soft X-ray Ratio of the HST-resolved Clouds* — Bianchi et al. (2006) studied a sample of eight Seyfert 2 galaxies, and suggested that the same kpc-scale gas photoionized by the AGN continuum can simultaneously produce the observed X-ray and [OIII] emission. Our HRC and ACIS studies of the inner $2''$ (< 130 pc) emission in NGC 4151 (Wang et al. 2009 and Paper II) have shown that, for most of the clouds close to the nucleus, the ratios of [OIII] to soft X-ray emission are consistent with the typical ratios in Bianchi et al. (2006), the exception being clouds collisionally ionized by the radio jet.

Our subpixel-processed ACIS images of NGC 4151 enable us to directly compare the extended X-ray emission and those of the resolved [OIII] clouds (Figure 6). The main cloud features are labeled in Figure 14. Using the calibrated continuum-subtracted HST/WFPC2 F502N image (Kaiser et al. 2000), we measured the [OIII] fluxes for the clouds and listed them in Table 3. ACIS spectra were extracted from the same regions and fitted with the continuum plus emission line model to obtain their 0.5–2 keV X-ray fluxes. Figure 15 shows the [OIII] to soft X-ray ratio for the distinct cloud features at various radii to the nucleus (~ 150 pc–1500 pc). The ratios listed in Table 3 are consistent with a constant [OIII]/X-ray flux ratio of ~ 15 for the 1.5 kpc range spanned by these measurements. The radially constant [OIII]/X-ray ratios indicate that the relative contributions of the low- and high-ionization gas phases at different radii are similar, as pointed out by our referee. If the [OIII] and X-ray emission arise from a single photoionized medium, as discussed in Bianchi et al. (2006), this further implies that the ionization parameter does not vary significantly to a large radial distance and the density is approximately decreasing as r^{-2} , as expected for a freely expanding nuclear wind based on mass conservation (Kraemer et al. 2000; Bianchi et al. 2006).

- *Spectral Fitting* — The spectral analysis shows that, a model with just two photoionized components of high- and low-ionization parameters can describe well the observed X-ray spectra in various regions across the circum-nuclear area, whereas in the spectral fits that invoke only collisionally ionized components strong emission line residuals persist. This supports the dominant role of nuclear photoionization.
- *Kinematics of the Ionized Gas* — The full velocity field of the NLR for NGC 4151 was mapped by Kaiser et al. (2000), which supports a hollow biconical outflow model for these clouds. At distances exceeding $4''$ (~ 260 pc) from the nucleus, Kaiser et al. (2000) find that the gas cloud kinematics are consistent with circular rotation in a

gravitational field, identical to the host ISM. Therefore, except for a few clouds in the nuclear region that appear disturbed by the impact of the radio jet (Kaiser et al. 2000; Mundell et al. 2003, see also Paper II), there is no evidence for strong kinematic shocks or any strong shocks in the outflow, which is consistent with the gas being photoionized by the nuclear radiation.

Based on all the above considerations, we conclude that photoionization by the nucleus is most likely the dominant ionization mechanism in the ENLR of NGC 4151, confirming the suggestions of previous studies (Ogle et al. 2000; Schurch et al. 2004; Kraemer et al. 2005; Armentrout et al. 2007; Wang et al. 2009b). It is reassuring to establish a role for nuclear photoionization in the extended NLRs that is consistent with the grating studies. However, there is also evidence that points to a more complex emission mechanism than a single photoionized medium (e.g., Bianchi et al. 2006). We discuss these results and their implications below in Sections 3.2 through 3.4.

3.1.2. Constraints on the Presence of Collisionally Ionized Gas

In § 2.2, we estimated the extent of thermal emission from hot gas ($L \lesssim 6 \times 10^{38}$ erg s $^{-1}$) that could be present in the circum-nuclear region of NGC 4151. The *Chandra* grating study of NGC 4151 by Ogle et al. (2000) provided the first direct evidence of X-ray line emission from a collisionally ionized hot plasma. Armentrout et al. (2007) also noted that the poor fit to the OVII line profile could be due to a non-photoionized component. Wang et al. (2011b) further show that a $kT \sim 0.6$ keV thermal emission component is present in the inner $r = 2''$ region, which likely originates from jet-cloud interaction.

Although star formation activity in the circum-nuclear region is at a low level (Asif et al. 2005; Dumas et al. 2010), hot gas may originate from the NGC 4151 galactic disk, since its temperature ($kT \sim 0.8$ keV) and luminosity ($L \sim 6 \times 10^{38}$) are comparable to the disk diffuse emission in some star forming galaxies, $kT \sim 0.6$ keV, $L \sim 10^{39}$ erg s $^{-1}$ (e.g., NGC 253; Strickland et al. 2002).

Another plausible alternative is that the hot plasma is the intercloud medium uniformly filling in the outflow (i.e., filling factor $f = 1$), providing pressure confinement for the NLR clouds (Elvis et al. 1983; cf. Krongold et al. 2007 for warm absorber outflows). The volume emission measure for the thermal component is $n_e^2 V = 4 \times 10^{61}$ cm $^{-3}$, derived from the normalization after fitting an additional thermal component (APEC) to the photoionization models of the bright biconical emission (§ 2.2.1). Assuming the hollow bi-conical NLR geometry (Crenshaw et al. 2000; Das et al. 2005), we obtain $V \sim 10^{61}$ cm $^{-3}$ and so an average

density of $\sim 2 \text{ cm}^{-3}$. Thus the thermal pressure of the $T \sim 10^7 \text{ K}$ gas is $\sim 5.5 \times 10^{-9} \text{ dyne cm}^{-2}$. Comparing with the thermal pressure of $T \sim 10^4 \text{ K}$ and $n = 1600 \text{ cm}^{-3}$ NLR clouds (Robinson et al. 1994) gives $p = 4.8 \times 10^{-9} \text{ dyne cm}^{-2}$. Thus pressure equilibrium between the hot and cool phase is highly likely, confirming the findings on pressure confinement in Ogle et al. (2000).

3.2. A Complex Photoionized Medium: Displacement of Optical and X-ray Features

Figure 6a clearly shows that one distinct OVII emission blob “A” (at $6''$, $\sim 390 \text{ pc}$ SW from the nucleus) does not align with a bright [OIII] emitting cloud, designated as “K1” in Robinson et al. (1994) and offset by $1''$ to the SE of “A” (see Yang et al. 2001). We find this is also the case for a more distant X-ray blob “B” ($10''$ SW) where the closest [OIII] emission cloud is $2''$ to the SW. Similar displacements between the X-ray enhancement and the [OIII] blob are also clearly found in the OVIII line emission (Figure 6b). Note that the *Chandra* astrometry is accurate to $0.3''$ (Paper I), therefore the mis-alignment between features at this spatial scale is significant and indicates that the origin of the optical/X-ray emission needs further investigation.

The radial location of X-ray blob “A” lies at the boundary between NLR and ENLR identified in the optical (Robinson et al. 1994), where the density drops rapidly from $n \sim 1600 \text{ cm}^{-3}$ to $n \sim 200 \text{ cm}^{-3}$ (Penston et al. 1990; Robinson et al. 1994). We can estimate the ionization parameter of K1. From the nuclear spectrum (Wang et al. 2010b), we obtain an ionizing luminosity $L_{13.6\text{eV}-100\text{keV}} \sim 10^{44} \text{ erg s}^{-1}$. Assuming a number density of 200 cm^{-3} (Penston et al. 1990; Robinson et al. 1994) and a radial distance of $1.2 \times 10^{21} \text{ cm}$ to the nucleus, we obtain an ionization parameter $\log U = -2$. This is lower than, but in agreement with, the value of $\log U \sim -1.7$ derived from the [OIII]/[OII] ratio in Robinson et al. (1994), supporting the photoionization assumption.

Since the X-ray blob and the [OIII] cloud are located at the same radial distance, their spatial offset suggests that the X-ray blob is in a higher ionization phase than the [OIII]-bright cloud. A likely explanation is that the X-ray blob has a lower density in the clump. If their densities are similar, the difference might arise from a higher ionizing flux received at the surface of the X-ray blob, perhaps due to less screening than in the direction towards the [OIII] cloud.

3.3. The Leaky “Torus”

Our spectral fitting results show that a range of ionization states are needed to obtain good fits, in agreement with the multiple ionization parameters required in the grating spectra (e.g., Armentrout et al. 2007).

A high ionization ($\log U \sim 1$) component is found in the spectral fitting for all regions surrounding the nucleus, including the NW and SE sectors perpendicular to the ionization cone (Table 2). A low ionization ($\log U \sim -1$) component is also present in the NW–SE direction that has lower U than found in the cone direction (NE–SW). This strongly indicates that there is no continuous absorbing “torus” blocking all the ionizing photons. This hypothesis is supported by the agreement between the observed H_2 line flux in the “torus” direction and the value predicted from X-ray-irradiation by the active nucleus (Paper I), and by the measurement of HI absorption in the nuclear region, where high levels of clumping on the smallest scales is found (Mundell et al. 2003). We note that a “patchy torus” or clumpy wind arising from the accretion disk in which the clouds are optically thick (e.g., Elitzur & Shlosman 2006), may allow leakage of nuclear continuum for such a high U component. However, it cannot reproduce the $\log U \sim -1$ component in the directions where the continuum is blocked.

Extended emission along the “torus” direction is clearly present in the large scale X-ray images shown in Figures 2 (indicated by the arrows) and 5a. The base of this emission is at the location of the nucleus, thus may indicate ionization by the leaked photons in this direction. Moreover, we found an intriguing coincidence between radial regions of enhanced X-ray surface brightness and the P.A. of outflowing optical clouds identified by the *HST* study (Das et al. 2005). They pointed out that these faint clouds flowing close to the plane of the torus would need to be ionized by leaked nuclear radiation, which is attested by our X-ray data. The low U suggests a lower ionizing flux received by some clouds, likely due to nuclear continuum filtered by “warm absorbers” (e.g., Krongold et al. 2007) or the cone walls (e.g., Kraemer et al. 2008). Evaluating the difference between the ionization parameters in the direction of torus and in the bicone, we estimate that approximately 1% of the total ionizing flux is seen by the NW–SE clouds.

3.4. AGN Interaction with the Host Galaxy Disk

Previous work on the NLR kinematics of NGC 4151 have established that the bi-cone geometry in NGC 4151 results in one side of the conical outflow exiting the galactic plane at a small angle, partly intersecting the host disk (e.g., Robinson et al. 1994; Crenshaw

et al. 2000; Das et al. 2005; Storch-Bergmann et al. 2009). Thus part of the host ISM is likely illuminated by the AGN radiation. Our X-ray work finds that multiple phases of photoionized gas are present in the ENLR of NGC 4151. The fitting results for the “OVII” rich (red in Figure 5) and “NeIX” rich (green in Figure 5) regions indicate that there is a range of ionizations, with a lower ionization phase associated with the clumpy clouds and the higher ionization with the diffuse outflow. There is a lowest ionization ($\log U \sim -2$) component at larger radii in the SW and NE sectors. This component may come from high density material in the host disk plane, perhaps the nuclear spirals, illuminated by the nuclear radiation.

We further note that interactions between the biconical outflow and the host galaxy ISM, similar to the radio jet–cloud interaction in the nuclear region, may contribute to the heating of any hot gas present in the host disk. Currently there is no evidence in the gas kinematics that supports any strong interaction (Kaiser et al. 2000). However, as we discuss below, there is some morphological evidence that, at the largest radii, the outflow runs into a clump in the inhomogeneous ISM and perhaps results in local shock heating of the gas.

Figure 16 gives a large scale (1 arcmin \times 1 arcmin) view of the key ISM components in the circum-nuclear region of NGC 4151, illustrating the directions of the kinematic major axis of the host galaxy (green solid line; P.A. $\sim 22^\circ$, Pedlar et al. 1992; Mundell et al. 1999), the large scale “weak fat bar” (green dotted line; P.A. $\sim 130^\circ$; Mundell & Shone 1999), the ENLR bicone (cyan line; P.A. $\sim 65^\circ$, Evans et al. 1993), and the distribution of HI (Mundell et al. 1999) and CO (Dumas et al. 2010) gas, respectively.

In Paper I we noted that the NE soft X-ray emission reaches as far as $12''$ (780 pc) from the nucleus, but that the surface brightness then decreases significantly by a factor of 5. Comparing the continuum-subtracted H α emission (Knapen et al. 2004) with the extended soft (0.3–1 keV) X-ray emission (Figure 17a), the ionized gas traced by bright H α emission is mainly located in the $r \sim 10''$ biconical region along the NE–SW direction centered on the nucleus, which also closely follows the soft X-ray emission. An arc-like feature in the H α image ($\sim 15'' \times 2''$) is clearly present at the $r = 10''$ location (Figure 16) at the edge of the X-ray emission, and the northern CO gas lane is also found here (Figure 17b, and Dumas et al. 2010).

Figure 17b provides a multiwavelength, enlarged view of this region, showing the spatial relations between the soft X-ray emission, the H α , the CO gas lanes, and the HI distribution (Mundell & Shone 1999). The termination of the NE X-ray emission appears to be closely associated with the presence of the dense cold neutral material (traced by the CO and HI emission) in the galactic disk. No similar feature is seen to the SW of the nucleus.

The origin of the $H\alpha$ arc (Figure 17a) at the terminus of the NE X-ray emission is intriguing. It is spatially very close to the northern CO gas lane and is one of the dust arcs identified in the optical $V - I$ color map (Asif et al. 1998), which are gaseous compressions driven by the bar potential (Mundell et al. 1999; Dumas et al. 2010). In this context, the $H\alpha$ arc may be a more clumpy continuation of the dense CO arc and photoionized by the AGN radiation. The rate of ionizing photons from the AGN is approximately 10^{53} s^{-1} (Kraemer et al. 2005; c.f. $L_{13.6\text{eV}-100\text{keV}} \sim 10^{44} \text{ erg s}^{-1}$, Wang et al. 2010b). Assuming that the arc has a line-of-sight depth that is comparable to its projected length ($\sim 1 \text{ kpc}$), the arc’s intercepted ionizing photon rate is $8 \times 10^{51} \text{ s}^{-1}$ at its distance to the nucleus (970 pc), a covering factor of almost 10%. This photon budget should be treated as an upper limit as some fraction of the ionization photons will be absorbed or scattered on the way to the arc. If we assume that the gas is in photoionization equilibrium, for the case B effective recombination rate of $H\alpha$ (Osterbrock 1989), a rate of $8 \times 10^{49} \text{ s}^{-1}$ ionizing photons s^{-1} is needed to produce the observed $H\alpha$ luminosity of the arc ($L_{H\alpha} \sim 8 \times 10^{37} \text{ erg s}^{-1}$), which is only 1% of the maximal rate of available ionizing radiation in the direction of the arc (for a covering factor $f_c = 10\%$). The scenario where part of the CO gas lane is photoionized by the AGN and produces the $H\alpha$ arc seems plausible with a modest covering factor of $f_c \sim 0.1\%$, implying that the arc has a filamentary structure with a thickness of a few pc.

On the other hand, we consider the possibility that the arc could be a bow shock feature from interaction between the biconical outflow and dense gas in the host disk piled in the CO gas lanes by the large scale stellar bar. Assuming that the X-ray emission is due to shock heating as the outflow encounters the dense CO lane, and that the shock is strong and adiabatic, we estimate the shock velocity v_s , adopting a postshock temperature $T_{ps} = (3/16)(\mu v_s^2/k_B)$ (Lehnert et al. 1999), where μ is the mass per particle (CO and HI) and k_B the Boltzmann constant. For the $kT \sim 0.3 \text{ keV}$ X-ray temperature measured at the arc, the required v_s is $\sim 150 \text{ km s}^{-1}$, which is much higher than the local sound speed $c_s = 10 \text{ km s}^{-1}$ in the $\sim 10^4 \text{ K}$ $H\alpha$ -emitting gas. Although there is no direct measurement at the exact position of the $H\alpha$ arc, the measured outflow velocity in [OIII] at $r = 8''$ NE of the nucleus is fully consistent with this value of v_s , e.g., cloud#28 which has $v = 190 \pm 32 \text{ km s}^{-1}$ (Kaiser et al. 2000).

3.5. Mass Outflow and Kinematic Power

For two of the brighter, spatially resolved [OIII]-emitting clouds seen in the *HST* images (clouds #1 and #2 in Figure 14; see also Figure 4 in Kaiser et al. 2000), we were able to constrain the number density for the X-ray emitting gas with *Cloudy* modeling of their X-

ray spectra when an inner radius $r = 100$ pc to the nucleus and an ionizing photon rate $Q = 10^{53}$ are set. The best-fit density is $\log n_H = 2.9 \pm 0.5 \text{ cm}^{-3}$. We use this number density to estimate the mass loss rate and the kinematic power of the hot phase outflow, which are key quantities that gauge the impact of AGN outflow on the host galaxy ISM.

Following Barbosa et al. (2009) and Storchi-Bergmann et al. (2010), we calculate the mass loss rate using $\dot{M}_x = n_H m_H v_r C_g A$, where v_r is the radial velocity (taken as the approximate outflow velocity), m_H the proton mass, C_g the gas filling factor, and A the area in the cross section of the outflow. For a radial distance of $r = 4 \times 10^{20}$ cm (130 pc) and the hollow cone geometry of Das et al. (2005), we obtain $A = \pi r^2 (\sin^2 \theta_{out} - \sin^2 \theta_{in}) = 1.2 \times 10^{40} \text{ cm}^2$. Adopting $C_g = 0.11$ (Storchi-Bergmann et al. 2010) and $v_r \sim 750 \text{ km s}^{-1}$ (Crenshaw et al. 2000; Storchi-Bergmann et al. 2010), we obtain a mass outflow rate $\dot{M}_x = 2.1 M_\odot \text{ yr}^{-1}$ and a kinetic luminosity for the outflow $L_{outflow} = 1/2 \dot{M}_x v^2 \sim 1.7 \times 10^{41} \text{ ergs s}^{-1}$, or $\sim 0.3\%$ of the bolometric luminosity of the AGN ($L_{bol} = 7.3 \times 10^{43} \text{ erg s}^{-1}$; Kaspi et al. 2005).

The \dot{M}_x derived from the hot phase outflow is comparable to the value derived from NIR studies of ionized gas in NGC 4151 (Storchi-Bergmann et al. 2010), which estimated mass outflow rate $\approx 1.2 M_\odot \text{ yr}^{-1}$ along each cone. The \dot{M}_x value is over 10 times higher than the outflow rate derived from UV and optical spectra ($0.16 M_\odot \text{ yr}^{-1}$; Crenshaw & Kraemer 2007), but the latter is measured much closer to the nucleus (at 0.1 pc). The optical emitting gas likely has a much smaller filling factor than the X-ray emitting gas, which explains the difference in the measurements. If our study measured an outer part of the same outflow, it could have accelerated to a higher velocity or have loaded ISM between 0.1 pc and 100 pc, hence a higher \dot{M}_x .

How does \dot{M}_x compare to the accretion rate of the SMBH in NGC 4151? The bolometric luminosity of NGC 4151, $L_{bol} = 7.3 \times 10^{43} \text{ erg s}^{-1}$ (Kaspi et al. 2005), is about 1.2% of its Eddington luminosity, which is $L_{Edd} \sim 6 \times 10^{45} \text{ erg s}^{-1}$ for the black hole mass $M_{BH} = 4.57_{-0.47}^{+0.57} \times 10^7 M_\odot$ of NGC 4151 (Bentz et al. 2006). Adopting $L_{bol} = \eta \dot{M}_{accr} c^2$ and $\eta = 0.1$ for the efficiency of the accretion disk (Shakura & Sunyaev 1973), this implies that the central engine of NGC 4151 is accreting at $\dot{M}_{accr} = 0.013 M_\odot \text{ yr}^{-1}$. Since the measured outflow rate is 160 times the accretion rate necessary to feed the active nucleus, there must be either significant entrainment of the host galaxy’s ISM while the nuclear outflow is expanding, or part of the gas fueling the nucleus is ejected before radiating, or a high fraction (over 99%) of the X-ray gas does not take part in the outflow and is illuminated by the AGN “in situ”. However, the latter seems unlikely as the grating spectra strongly indicate that the emission lines have outflow velocities of 200–300 km s^{-1} (e.g., Armentrout et al. 2007). Significant mass loading of the outflow by the host ISM may be most plausible and common, since previous estimated NLR outflow rates in Seyferts ($\sim 0.1\text{--}10 M_\odot \text{ yr}^{-1}$)

generally exceed tenfold the accretion rate (Veilleux et al. 2005).

Nevertheless, even with such a high \dot{M}_x in NGC 4151, the kinematic power $L_{outflow}$ suggests that only 0.3% of the available accretion power is extracted to drive the outflow, similar to the findings of Storchi-Bergmann et al. (2010) and Holt et al. (2006, 2011). For a sample of Seyfert NLR outflows (NGC 4151 not included) studied in the [SIII] λ 9069 emission, Barbosa et al. (2009) reported a lower $L_{outflow}/L_{bol} = 10^{-5} - 10^{-4}$. As pointed out in Mathur et al. (2009), this poses a problem to the majority of quasar feedback models which require a higher fraction of the accretion power of the black hole ($\sim 5\%$ of L_{bol} to unity) to be thermally coupled to the host ISM. Our $L_{outflow}/L_{bol}$ is in rough agreement with a two-stage feedback model recently proposed by Hopkins & Elvis (2010), which requires only 0.5% of the radiated energy to drive the initial hot outflow to efficiently shut down star formation in the host.

4. Conclusions

In this paper we present spectral analysis and emission line images from deep *Chandra* observation of NGC 4151, aiming to resolve and characterise the X-ray emission in the NLR. The findings are summarized as follows:

- The soft X-ray emission line images of NGC 4151 (OVII, OVIII, and NeIX) are clearly extended and show remarkable morphological coincidence with the biconical NLR mapped by the [OIII] emission, which supports a common emission mechanism for the hot- and cool-phase of the NLR gas.
- Extended emission in the X-ray image is detected along the NW–SE sectors, which is the direction of a putative torus. This may explain the faint rogue clouds identified in previous HST studies that require ionization in this direction, indicating leakage of nuclear ionization instead of full blocking by a continuous obscuring torus.
- Spectral models involving smooth continua (a bremsstrahlung plus a power law) with emission lines provide good descriptions of the spectra. The emission lines cannot be uniquely identified with the present spectral resolution, but are consistent with the brighter lines seen in the *Chandra* HETGS and XMM-Newton RGS spectra below 2 keV. The absorption corrected X-ray luminosity of the extended emission between $r = 130$ pc and $r = 2$ kpc is $L_{0.3-2\text{keV}} = 1.1 \pm 0.2 \times 10^{40} \text{ erg s}^{-1}$.
- Photoionization models successfully reproduce the soft X-ray emission, supporting the dominant role of nuclear photoionization. There are considerable variations in ionization states across the circum-nuclear region. A high ionization ($\log U \sim 1$) component

is present in most regions. A low ionization ($\log U \sim -0.25$) component is present along the bicone direction (NE–SW), whereas a lower ionization ($\log U \sim -1$) component is found in the NW–SE direction, which is consistent with filtered nuclear emission by warm absorbers instead of a continuous absorbing torus. The lowest ionization component ($\log U \sim -2$) appears to be associated with the dense gas in the host plane. A thermal component may still be present at $\lesssim 12\%$ of the total soft emission, perhaps related to hot ISM in the galactic disk or shocks associated with the outflow.

- The measured ratios of [OIII]/soft X-ray flux are consistent with a constant ratio of ~ 15 for the 1.5 kpc radius spanned by these measurements. This suggests a similar relative contributions from the low- and high-ionization gas phases at different radii. If the [OIII] and X-ray emission arise from a single photoionized medium, this further implies an outflow with a wind-like density profile ($n_e \propto r^{-2}$).
- The estimated mass outflow rate in NGC 4151 is $\sim 2M_\odot \text{ yr}^{-1}$ at 130 pc and the kinematic power of the ionized outflow is $1.7 \times 10^{41} \text{ erg s}^{-1}$, $0.3\% L_{bol}$. This value is significantly lower than the expected efficiency in the majority of quasar feedback models, but comparable to the two-stage model described in Hopkins & Elvis (2010).

Placing all our findings in the context of previous studies, we obtain a comprehensive view of the NGC 4151 circum-nuclear region at various spatial scales, from the inner-most $r \sim 50 \text{ pc}$ (as illustrated in the schematic drawing in Figure 18a) to as far as $r \sim 2 \text{ kpc}$ (Figure 18b). The key points are recapped here.

Photoionization by the nucleus is important at all scales. In the nuclear region, except for a few clouds that show interaction with the radio jet (Wang et al. 2009, 2011b), most of the X-ray NLR clouds are consistent with being part of a photoionized biconical outflow, with a $n \propto r^{-2}$ density profile expected for a nuclear wind.

In the ENLR of NGC 4151, photoionization is still the dominant ionization mechanism for the observed X-ray emission (e.g., Ogle et al. 2000; Kraemer et al. 2005), but a wide range of ionization states is present. This is likely related to the nature of the ENLR. The bi-cone geometry indicates that one side of the conical outflow exits the galactic plane at a small angle, partly intersecting the host disk (e.g., Crenshaw et al. 2000; Das et al. 2005; Storchi-Bergmann et al. 2010). Optical studies (e.g., Robinson et al. 1994; Kaiser et al. 2000) have identified such a boundary between NLR and ENLR at $r \approx 6''$ (SW), and the ionized gas kinematics become consistent with the rotation velocity of the galactic disk at $r \geq 6''$. Thus the origin of the ENLR is best explained as the inhomogeneous ISM in the galactic plane ionized by the AGN. Part of the high density nuclear spirals illuminated in the path of the bicone can produce the curvy shape of X-ray enhancement and the associated

low ionization. The presence of ionized emission perpendicular to the bicone indicates leaked nuclear emission along the putative torus direction, likely filtered nuclear emission by warm absorbers.

In the large 3 kpc-scale cavity of the H I material, we find faint soft diffuse X-ray emission that provides evidence for AGN–host interaction in NGC 4151 (Wang et al. 2010a), originated from either hot gas heated by the nuclear outflow or photoionized gas from a recent nuclear outburst.

As a concluding remark, our findings in NGC 4151 demonstrate that abundant information can be extracted from X-ray spectral imaging studies when supplemented with multiwavelength data. Many valuable new radio, optical and IR observations and modeling of other nearby Seyfert galaxies are emerging (Crenshaw et al. 2010; Riffel et al. 2010; Fisher et al. 2011, Schnorr Müller et al. 2011), and progress in the X-rays are being made to further our understanding of AGN feeding and feedback processes in these galaxies.

We thank the anonymous referees for providing us with detailed and constructive comments that have improved the clarity of this manuscript. This work is supported by NASA grant GO8-9101X and GO1-12009X. We acknowledge support from the CXC, which is operated by the Smithsonian Astrophysical Observatory (SAO) for and on behalf of NASA under Contract NAS8-03060. CGM acknowledges financial support from the Royal Society and Research Councils U.K. GD was supported by DFG grants SCH 536/4-1 and SCH 536/4-2 as part of SPP 1177. J. W. thanks T. Kallman, G. Ferland, S. Bianchi, A. Marinucci, and S. Chakravorty for advice on photoionization modeling. This research has made use of data obtained from the *Chandra* Data Archive, and software provided by the CXC in the application packages CIAO and Sherpa. Some of the data presented in this paper were obtained from the Multimission Archive at the Space Telescope Science Institute (MAST). STScI is operated by the Association of Universities for Research in Astronomy, Inc., under NASA contract NAS5-26555.

Facilities: CXO (HRC, ACIS)

REFERENCES

- Armentrout, B. K., Kraemer, S. B., & Turner, T. J. 2007, *ApJ*, 665, 237
- Arnaud, K. A. 1996, *Astronomical Data Analysis Software and Systems V*, 101, 17

- Asif, M. W., Mundell, C. G., Pedlar, A., Unger, S. W., Robinson, A., Vila-Vilaro, B., & Lewis, J. R. 1998, *A&A*, 333, 466
- Asif, M. W., Mundell, C. G., & Pedlar, A. 2005, *MNRAS*, 359, 408
- Barbosa, F. K. B., Storchi-Bergmann, T., Cid Fernandes, R., Winge, C., & Schmitt, H. 2009, *MNRAS*, 396, 2
- Bentz, M. C., et al. 2006, *ApJ*, 651, 775
- Bianchi, S., Guainazzi, M., & Chiaberge, M. 2006, *A&A*, 448, 499
- Bianchi, S., Chiaberge, M., Evans, D. A., Guainazzi, M., Baldi, R. D., Matt, G., & Piconcelli, E. 2010, *MNRAS*, 405, 553
- Crenshaw, D. M., et al. 2000, *AJ*, 120, 1731
- Crenshaw, D. M., & Kraemer, S. B. 2007, *ApJ*, 659, 250
- Crenshaw, D. M., Kraemer, S. B., Schmitt, H. R., Jaffé, Y. L., Deo, R. P., Collins, N. R., & Fischer, T. C. 2010, *AJ*, 139, 871
- Das, V., et al. 2005, *AJ*, 130, 945
- de Rosa, A., Piro, L., Perola, G. C., Capalbi, M., Cappi, M., Grandi, P., Maraschi, L., & Petrucci, P. O. 2007, *A&A*, 463, 903
- Dumas, G., Schinnerer, E., & Mundell, C. G. 2010, *ApJ*, in press, astro-ph/1008.0856
- Elitzur, M., & Shlosman, I. 2006, *ApJ*, 648, L101
- Elvis, M., Briel, U. G., & Henry, J. P. 1983, *ApJ*, 268, 105
- Elvis, M., Fassnacht, C., Wilson, A. S., & Briel, U. 1990, *ApJ*, 361, 459
- Evans, I. N., Tsvetanov, Z., Kriss, G. A., Ford, H. C., Caganoff, S., & Koratkar, A. P. 1993, *ApJ*, 417, 82
- Ferland, G. J., Korista, K. T., Verner, D. A., Ferguson, J. W., Kingdon, J. B., & Verner, E. M. 1998, *PASP*, 110, 761
- Fischer, T. C., Crenshaw, D. M., Kraemer, S. B., Schmitt, H. R., Mushotsky, R. F., & Dunn, J. P. 2011, *ApJ*, 727, 71

- Garmire, G. P., Bautz, M. W., Ford, P. G., Nousek, J. A., & Ricker, G. R., Jr. 2003, *Proc. SPIE*, 4851, 28
- González-Martín, O., 2008, PhD Thesis, Instituto de Astrofísica de Andalucía, Granada, Spain
- Gonzalez-Martin, O., Acosta-Pulido, J. A., Perez Garcia, A. M., & Ramos Almeida, C. 2010, *ApJ*, 723, 1748
- Guainazzi, M., Risaliti, G., Nucita, A., Wang, J., Bianchi, S., Soria, R., & Zezas, A. 2009, *A&A*, 505, 589
- Heckman, T. M., & Balick, B. 1983, *ApJ*, 268, 102
- Holt, J., Tadhunter, C., Morganti, R., Bellamy, M., González Delgado, R. M., Tzioumis, A., & Inskip, K. J. 2006, *MNRAS*, 370, 1633
- Holt, J., Tadhunter, C. N., Morganti, R., & Emonts, B. H. C. 2011, *MNRAS*, 410, 1527
- Hopkins, P. F., & Elvis, M. 2010, *MNRAS*, 401, 7
- Kaiser, M. E., et al. 2000, *ApJ*, 528, 260
- Kaspi, S., Maoz, D., Netzer, H., Peterson, B. M., Vestergaard, M., & Jannuzi, B. T. 2005, *ApJ*, 629, 61
- Kinkhabwala, A., et al. 2002, *ApJ*, 575, 732
- Kinkhabwala, A., Behar, E., Sako, M., Gu, M. F., Kahn, S. M., & Paerels, F. B. S. 2003, *arXiv:astro-ph/0304332*
- Knapen, J. H., Stedman, S., Bramich, D. M., Folkes, S. L., & Bradley, T. R. 2004, *A&A*, 426, 1135
- Komossa, S. 2001, *A&A*, 371, 507
- Kraemer, S. B., et al. 2005, *ApJ*, 633, 693
- Kraemer, S. B., Schmitt, H. R., & Crenshaw, D. M. 2008, *ApJ*, 679, 1128
- Krongold, Y., Nicastro, F., Elvis, M., Brickhouse, N., Binette, L., Mathur, S., & Jiménez-Bailón, E. 2007, *ApJ*, 659, 1022
- Lehnert, M. D., Heckman, T. M., & Weaver, K. A. 1999, *ApJ*, 523, 575

- Liedahl, D. A. 1999, *X-Ray Spectroscopy in Astrophysics*, 520, 189
- Lubinski, P., Zdziarski, A. A., Walter, R., Paltani, S., Beckmann, V., Soldi, S., Ferrigno, C., & Courvoisier, T. J. -. 2010, arXiv:1005.0842
- Mathur, S., Stoll, R., Krongold, Y., Nicastro, F., Brickhouse, N., & Elvis, M. 2009, *American Institute of Physics Conference Series*, 1201, 33
- Morse, J. A., Wilson, A. S., Elvis, M., & Weaver, K. A. 1995, *ApJ*, 439, 121
- Murphy, E. M., Lockman, F. J., Laor, A., & Elvis, M. 1996, *ApJS*, 105, 369
- Mundell, C. G., Wrobel, J. M., Pedlar, A., & Gallimore, J. F. 2003, *ApJ*, 583, 192
- Mundell, C. G., & Shone, D. L. 1999, *MNRAS*, 304, 475
- Mundell, C. G., Pedlar, A., Shone, D. L., & Robinson, A. 1999, *MNRAS*, 304, 481
- Ogle, P. M., Marshall, H. L., Lee, J. C., & Canizares, C. R. 2000, *ApJ*, 545, L81
- Ogle, P. M., Brookings, T., Canizares, C. R., Lee, J. C., & Marshall, H. L. 2003, *A&A*, 402, 849
- Osterbrock, D. E. 1989, *Astrophysics of gaseous nebulae and active galactic nuclei*, Mill Valley, University Science Books
- Osterbrock, D. E., & Ferland, G. J. 2006, *Astrophysics of gaseous nebulae and active galactic nuclei*, 2nd. ed. by D.E. Osterbrock and G.J. Ferland. Sausalito, CA: University Science Books, 2006,
- Pedlar, A., Howley, P., Axon, D. J., & Unger, S. W. 1992, *MNRAS*, 259, 369
- Penston, M. V., et al. 1990, *A&A*, 236, 53
- Perez, E., Gonzalez-Delgado, R., Tadhunter, C., & Tsvetanov, Z. 1989, *MNRAS*, 241, 31P
- Porter, R. L., Ferland, G. J., Kraemer, S. B., Armentrout, B. K., Arnaud, K. A., & Turner, T. J. 2006, *PASP*, 118, 920
- Riffel, R. A., Storchi-Bergmann, T., & Nagar, N. M. 2010, *MNRAS*, 404, 166
- Robinson, A., et al. 1994, *A&A*, 291, 351
- Schnorr Müller, A., Storchi-Bergmann, T., Riffel, R. A., Ferrari, F., Steiner, J. E., Axon, D. J., & Robinson, A. 2011, *MNRAS*, 62

- Schulz, H., & Komossa, S. 1993, *A&A*, 278, 29
- Schurch, N. J., Warwick, R. S., Griffiths, R. E., & Kahn, S. M. 2004, *MNRAS*, 350, 1
- Shakura, N. I., & Sunyaev, R. A. 1973, *A&A*, 24, 337
- Smith, R. K., Brickhouse, N. S., Liedahl, D. A., & Raymond, J. C. 2001, *ApJ*, 556, L91
- Strickland, D. K., Heckman, T. M., Weaver, K. A., Hoopes, C. G., & Dahlem, M. 2002, *ApJ*, 568, 689
- Storchi-Bergmann, T., McGregor, P. J., Riffel, R. A., Simões Lopes, R., Beck, T., & Dopita, M. 2009, *MNRAS*, 394, 1148
- Storchi-Bergmann, T., Lopes, R. D. S., McGregor, P. J., Riffel, R. A., Beck, T., & Martini, P. 2010, *MNRAS*, 402, 819
- Unger, S. W., Pedlar, A., Axon, D. J., Whittle, M., Meurs, E. J. A., & Ward, M. J. 1987, *MNRAS*, 228, 671
- Veilleux, S., Cecil, G., & Bland-Hawthorn, J. 2005, *ARA&A*, 43, 769
- Wang, J., Fabbiano, G., Karovska, M., Elvis, M., Risaliti, G., Zezas, A., & Mundell, C. G. 2009, *ApJ*, 704, 1195
- Wang, J., Fabbiano, G., Risaliti, G., Elvis, M., Mundell, C. G., Dumas, G., Schinnerer, E., & Zezas, A. 2010a, *ApJ*, 719, L208
- Wang, J., Risaliti, G., Fabbiano, G., Elvis, M., Zezas, A., & Karovska, M. 2010b, *ApJ*, 714, 1497
- Wang, J., et al. 2011a, *ApJ*, 729, 75
- Wang, J., et al. 2011b, Submitted to *ApJ*, astro-ph/1103.1912
- Weaver, K. A., et al. 1994, *ApJ*, 423, 621
- Yang, Y., Wilson, A. S., & Ferruit, P. 2001, *ApJ*, 563, 124
- Young, A. J., Wilson, A. S., & Shopbell, P. L. 2001, *ApJ*, 556, 6

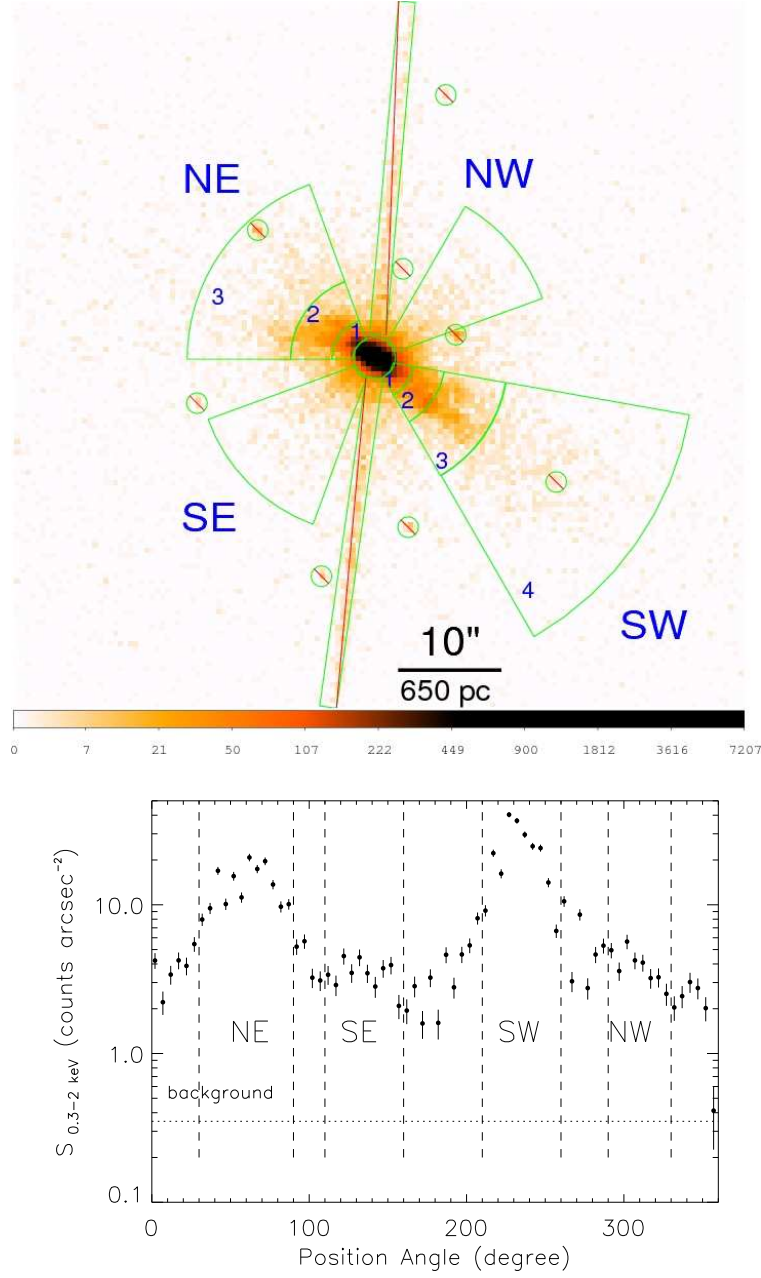


Fig. 1.— (a) Extraction regions of the large scale extended emission superposed on a gray-scale ACIS 0.3–2 keV band image. Excluded point sources are indicated by circles. The readout streaks running in the north-south direction is indicated. (b) The azimuthal surface brightness profile of the 0.3–2 keV emission, outlining sectors that contain bright extended emission.

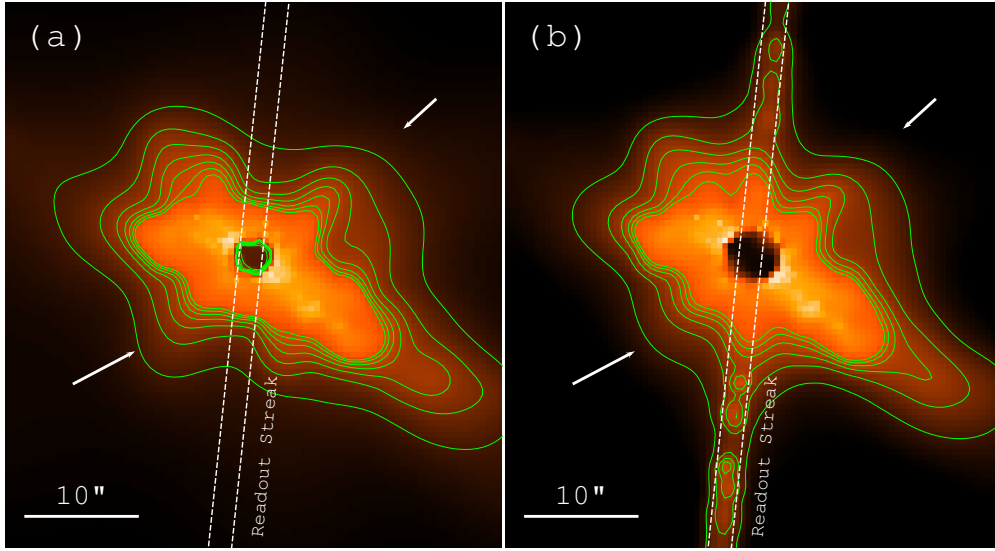


Fig. 2.— (a) Adaptively smoothed ACIS image (0.3–2 keV) of the central 3 kpc-diameter region of NGC 4151. (b) Same as (a), but here the readout streaks are not removed, in order to avoid artificially increasing the significance of the NW–SE extension (indicated by the arrows). The contours are overlaid to help visualize the extent of the diffuse emission. The brightest nuclear region is masked.

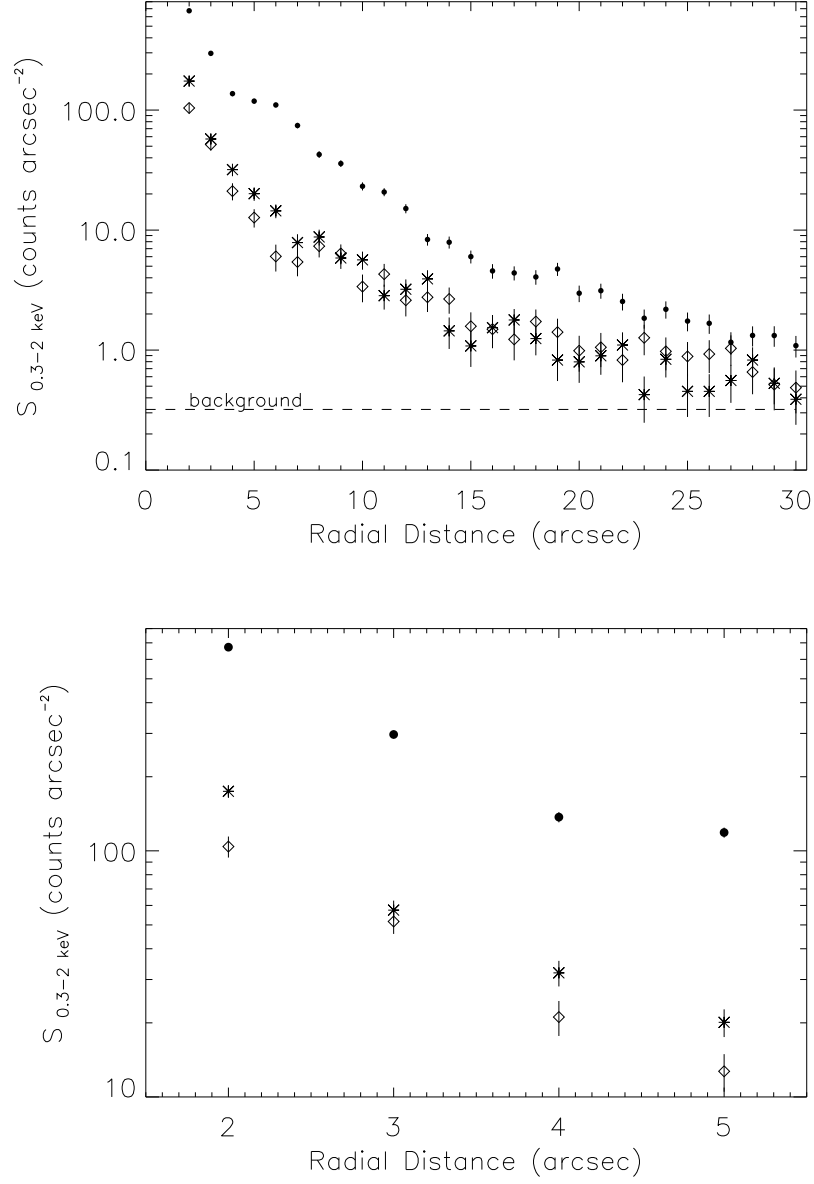


Fig. 3.— (a) Comparison of the radial profiles of the bright SW cone (dots), the NW sector (asterisk), and the region in between (along $P.A. \sim 270^\circ$; diamond). (b) Same as (a) but emphasizing the differences in the inner 5 arcsec region.

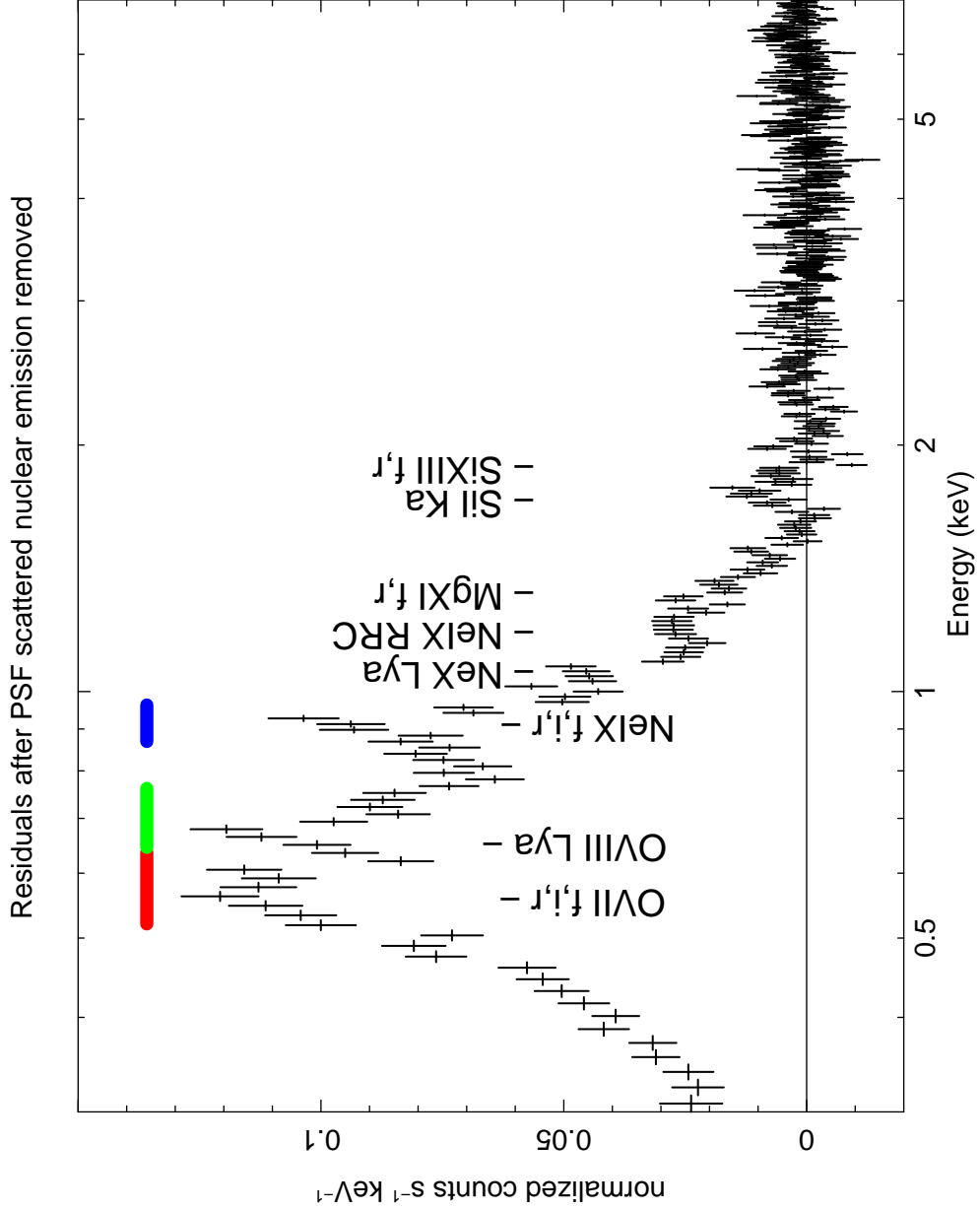


Fig. 4.— The residual spectrum of the large scale extended emission in NGC 4151 after the contribution from nuclear emission has been removed, demonstrating the presence of X-ray emission lines. Positions of the strong lines from the Ogle et al. (2000) HETG spectra are labelled, although they are blended at the spectral resolution of ACIS. The color bars outline the ranges used for narrow-band line images.

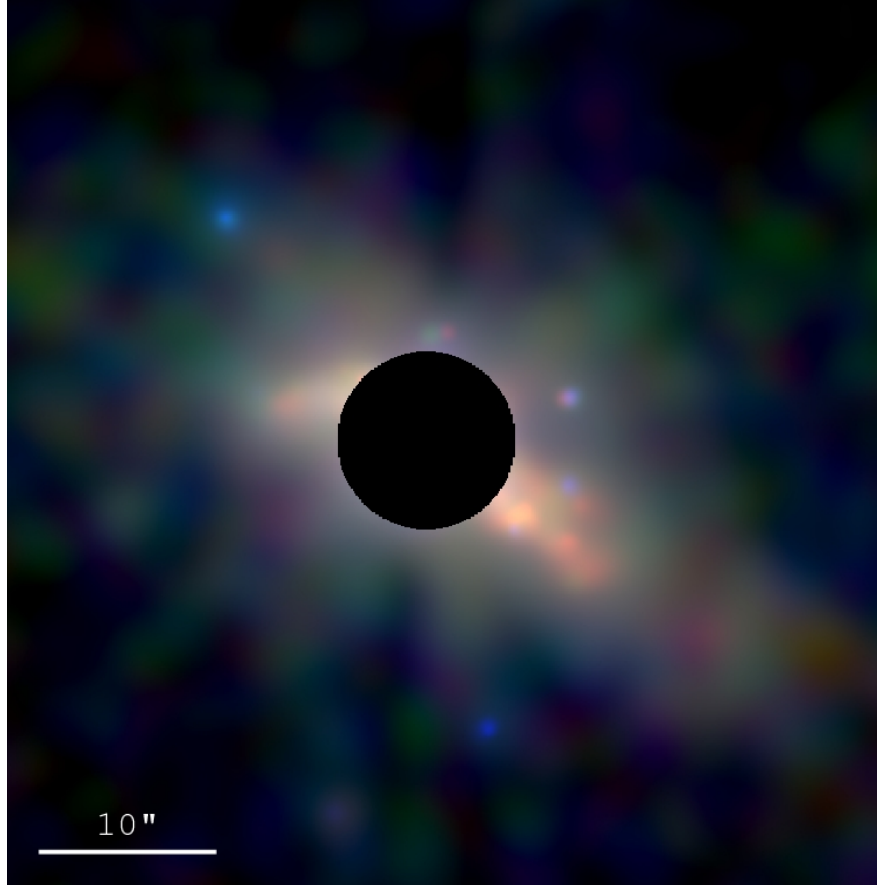


Fig. 5.— (a) Tri-color composite image of the central 3 kpc-diameter region of NGC 4151, where the soft (0.3–0.7 keV), medium (0.7–1 keV), and hard band (1–2 keV) adaptively smoothed images are shown in red, green, and blue, respectively. The inner $r = 5''$ region is intentionally saturated and masked to show the faint features farther out. (b) Same as Figure 5, but for the inner 1 kpc-radius region of NGC 4151. The inner $r = 2''$ nuclear region is masked.

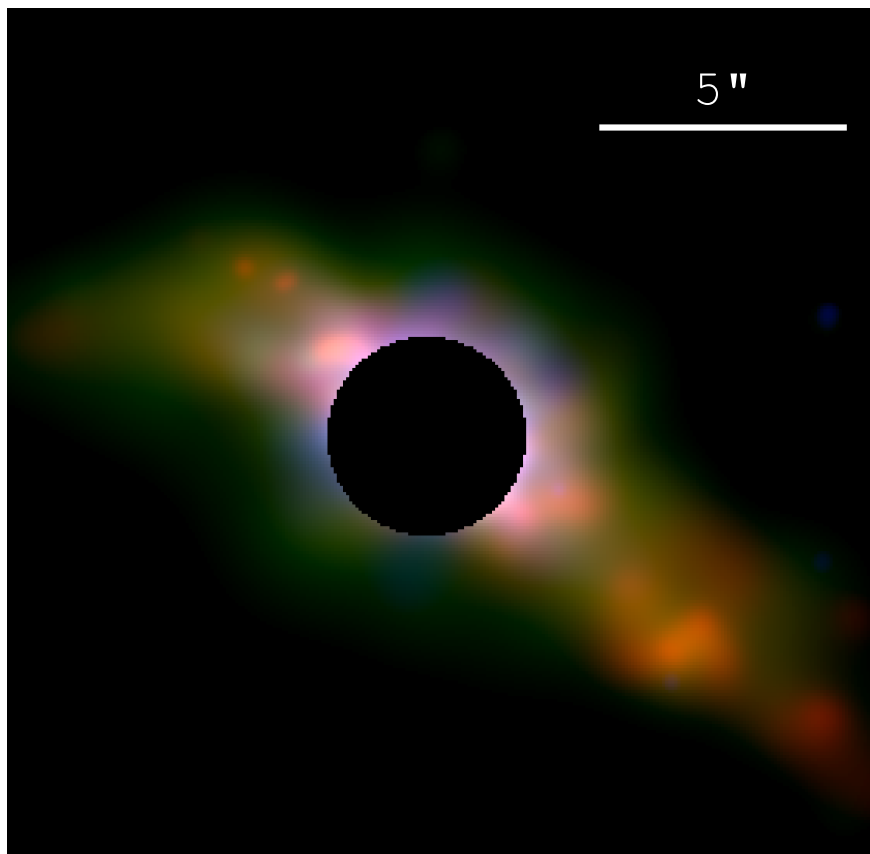


Fig. 5.— —Continued.

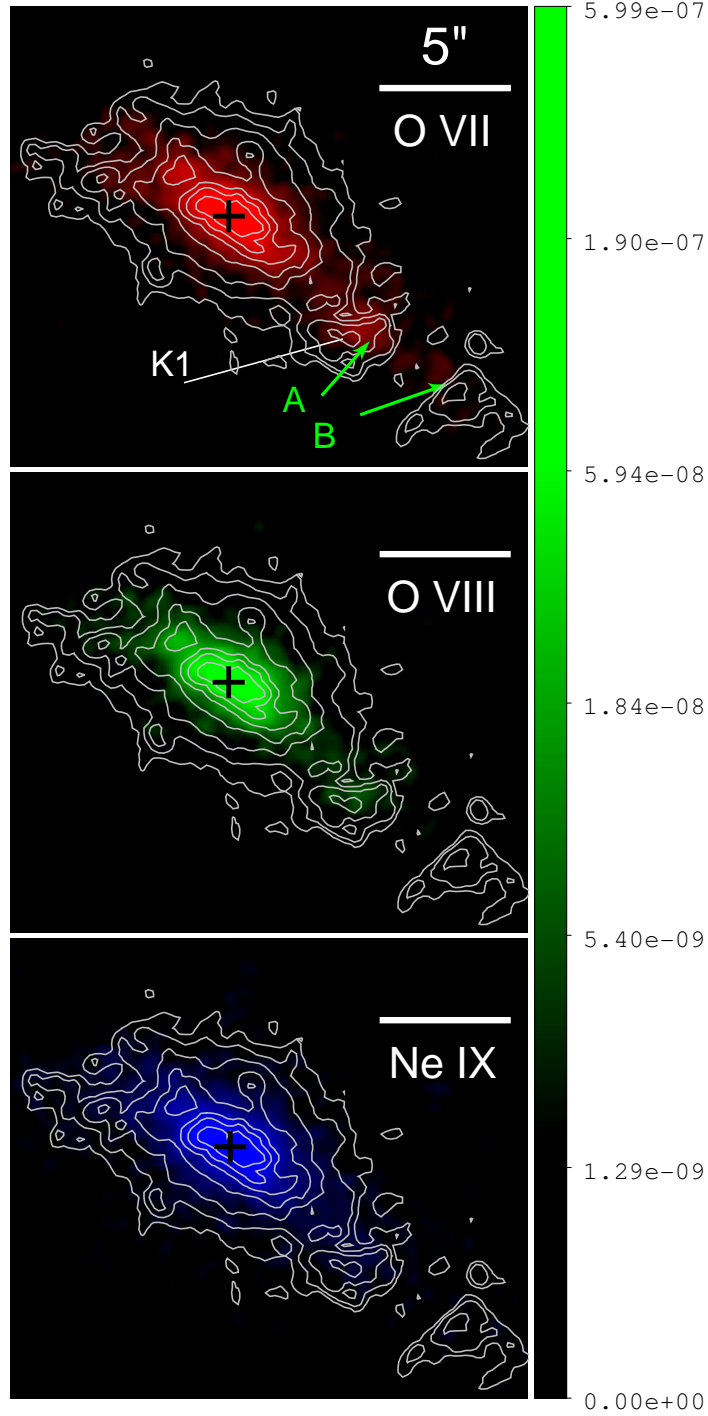


Fig. 6.— The narrow-band ACIS images of the three strongest emission features in the central 15'' (~ 1 kpc-across) region of NGC 4151 (a) OVII; (b) OVIII Ly α +OVII RRC; (c) NeIX OVII triplet line emission. Overlaid are contours of the *HST* WFPC2 [OIII] $\lambda 5007\text{\AA}$ image (Kaiser et al. 2000). The position of nucleus is indicated with a cross. “A” and “B” mark the X-ray structures displaced from optical clouds. “K1” is a bright [OIII] cloud identified in Robinson et al. (1994). See § 3.2. (d) The radial profile comparison for the emission line fluxes with $1\text{-}\sigma$ error bars, including the weaker emission lines NeX and Mg XI (see the legend in the top-left panel).

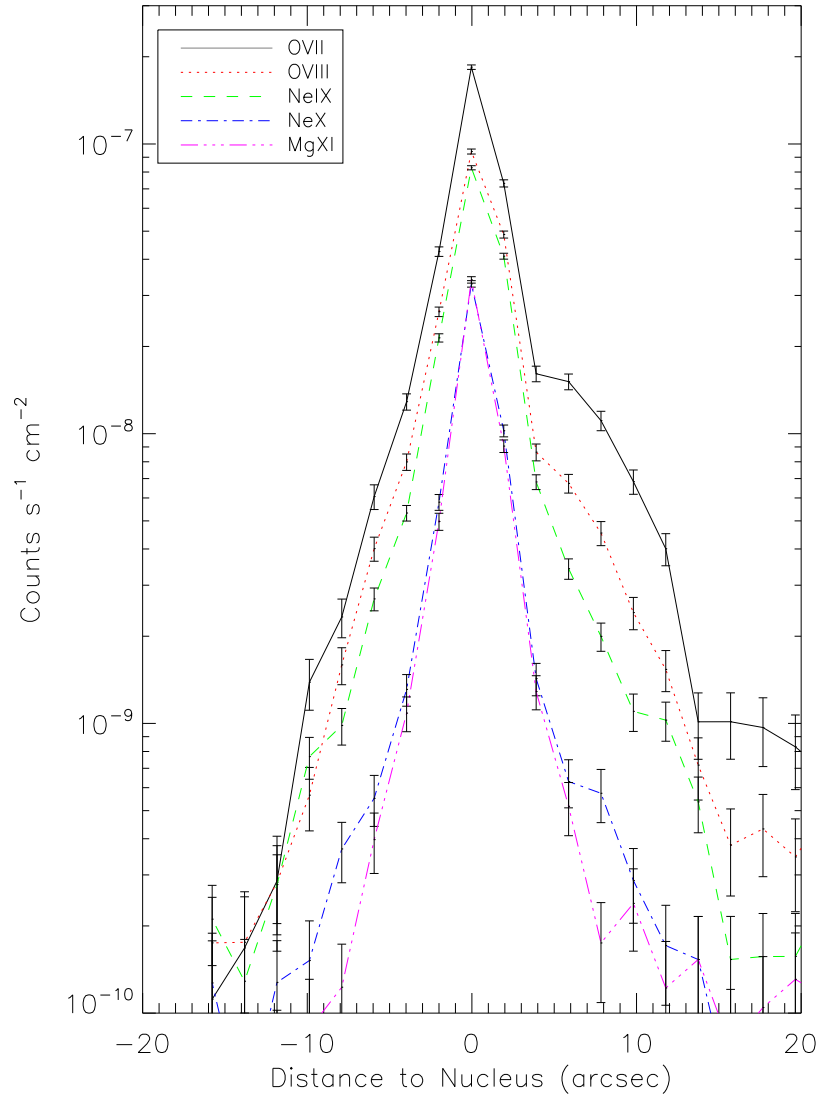


Fig. 6.— —Continued.

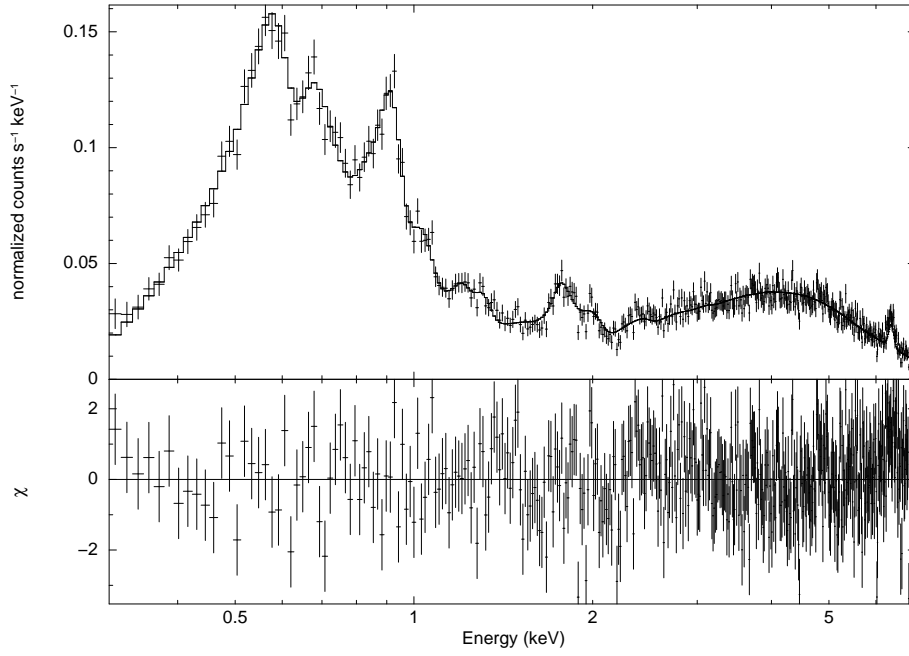


Fig. 7.— Spectrum of the extended X-ray emission with the best-fit phenomenological model consisting of a Bremsstrahlung component and gaussian lines, with lower panel showing the bin-to-bin contribution to the χ^2 statistics.

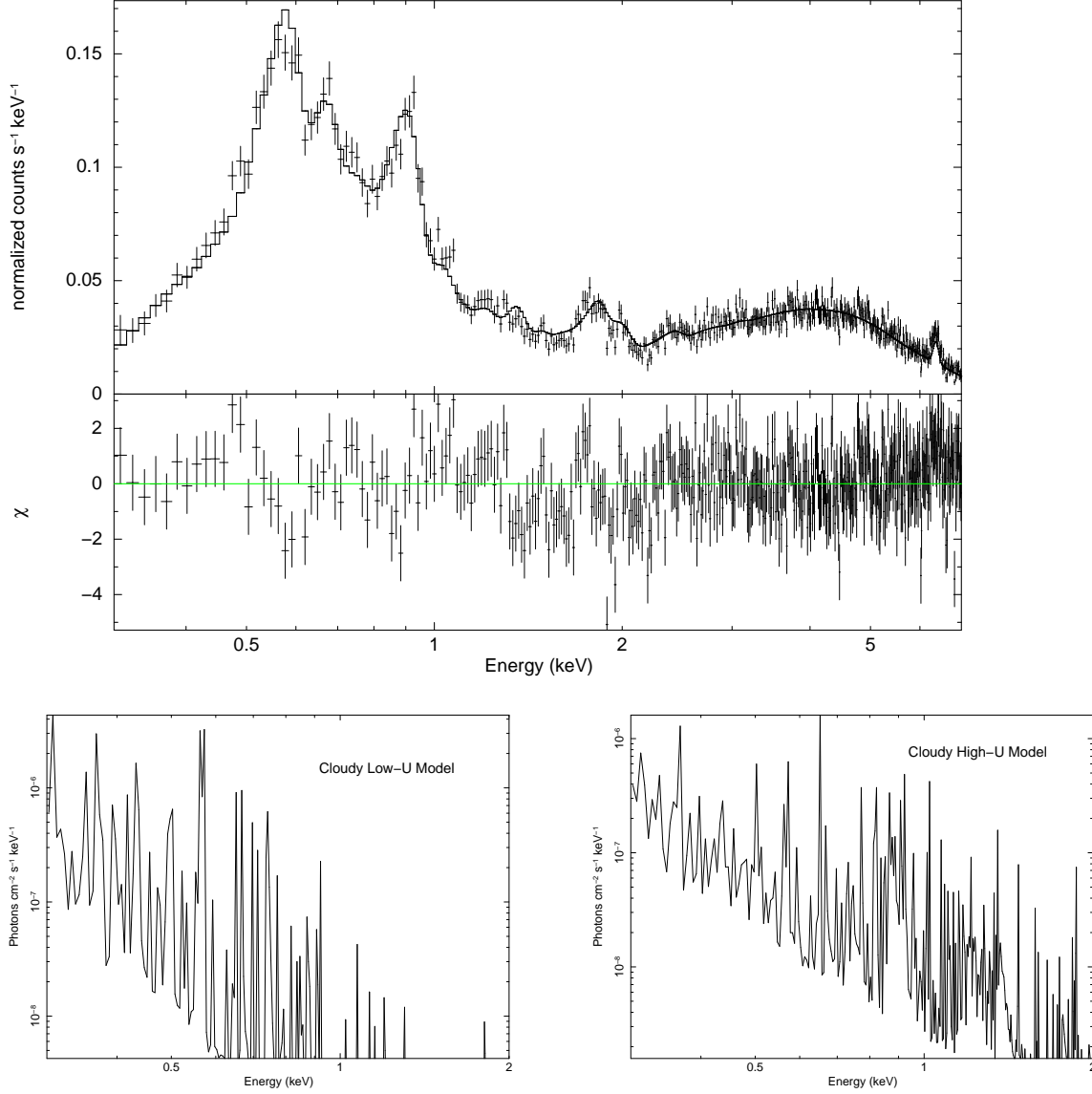


Fig. 8.— (a) The same spectrum as shown in Figure 7, but with the best fit spectral model consisting of two photoionized components. (b)-(c) The photoionized models calculated by **Cloudy** for the low ionization parameter ($\log U = -0.25$) and the high ionization parameter ($\log U = 0.8$) component, respectively.

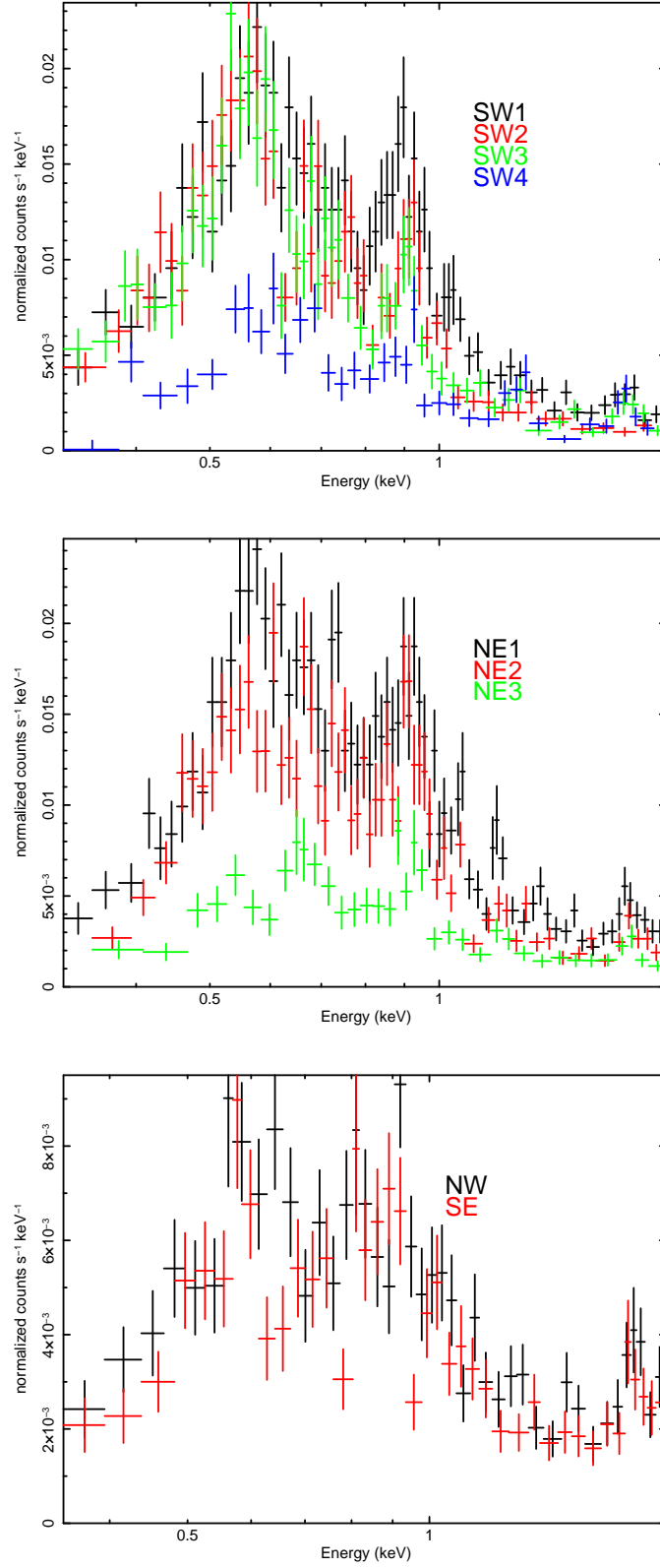


Fig. 9.— Comparison of the ACIS spectra across sectors and radially binned sub-regions (see Figure 1), demonstrating the spectral differences. (a) the SW cone; (b) the NE cone; (c) the NW and SE sectors that are perpendicular to the bicone.

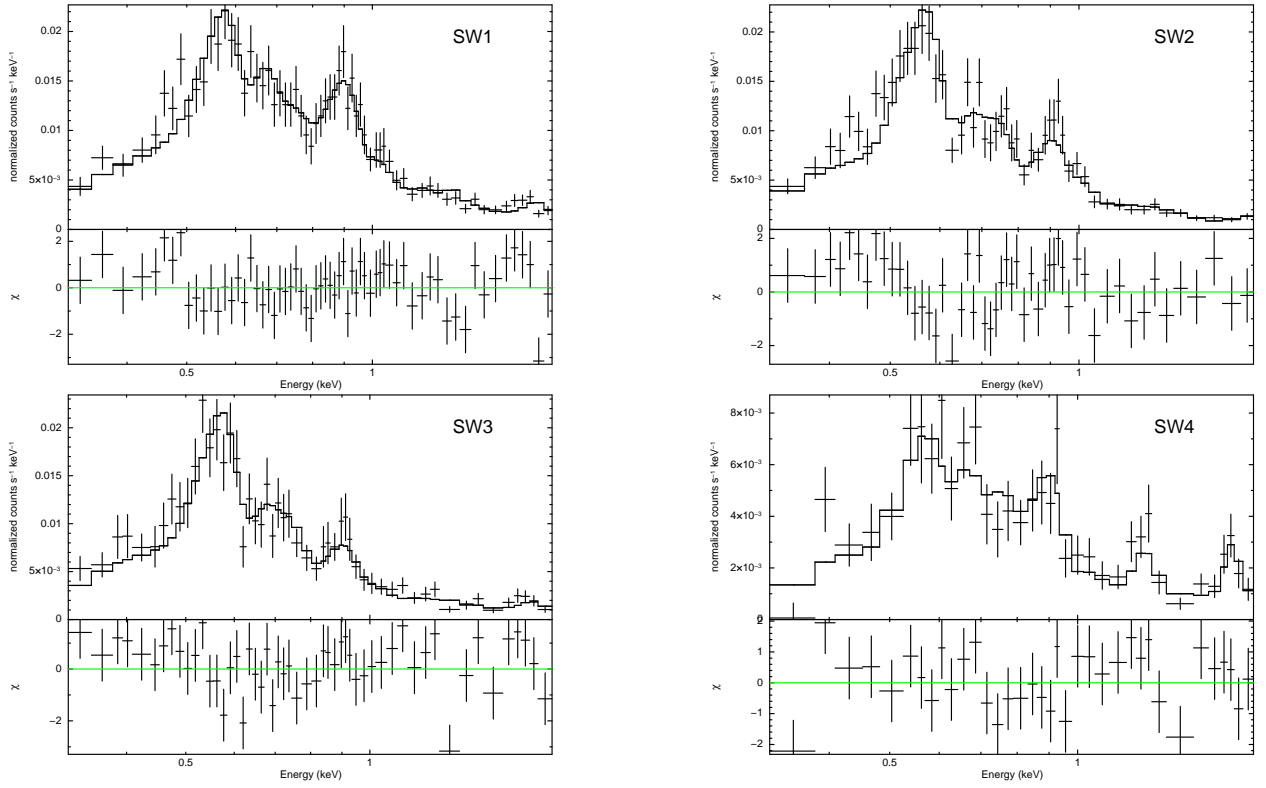


Fig. 10.— (a)-(d): Spectra of the X-ray emission in four regions radially separated along the SW sector (see Figure 1).

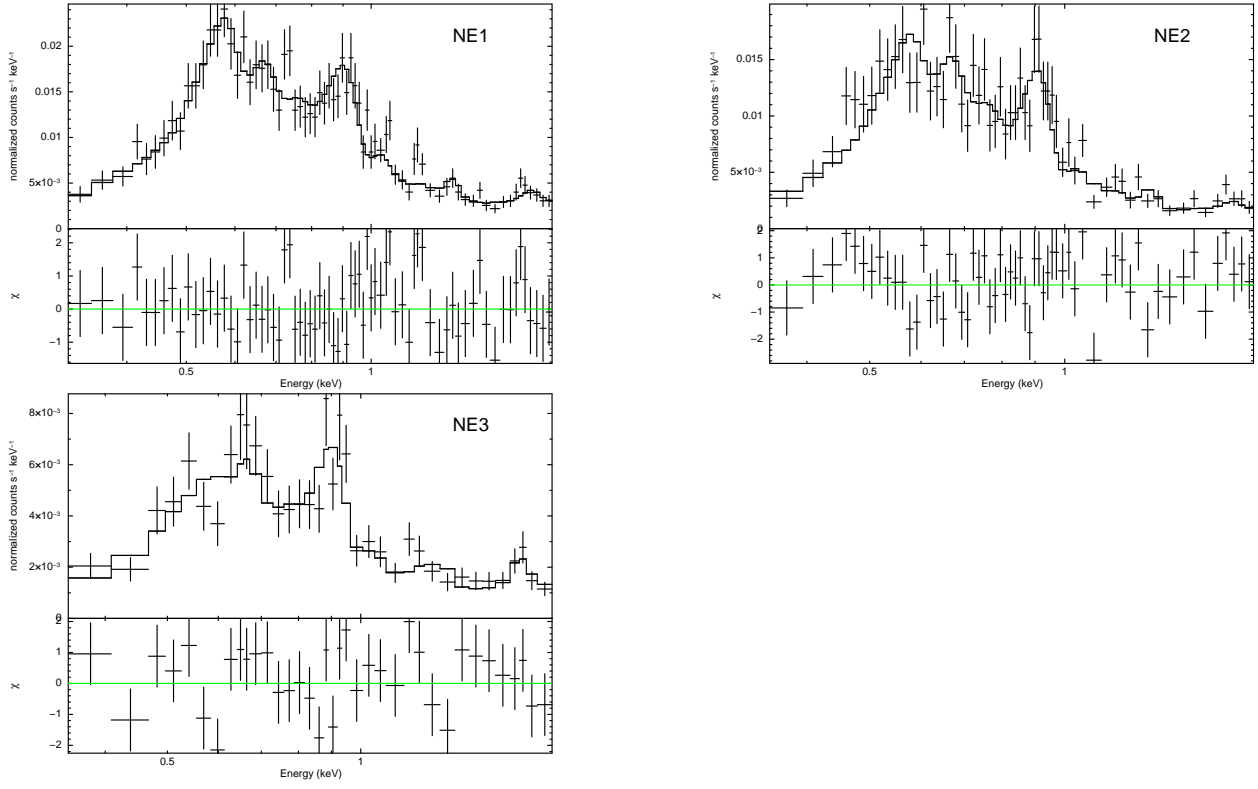


Fig. 11.— (a)-(c): Spectra of the X-ray emission in three regions radially along the NE sector.

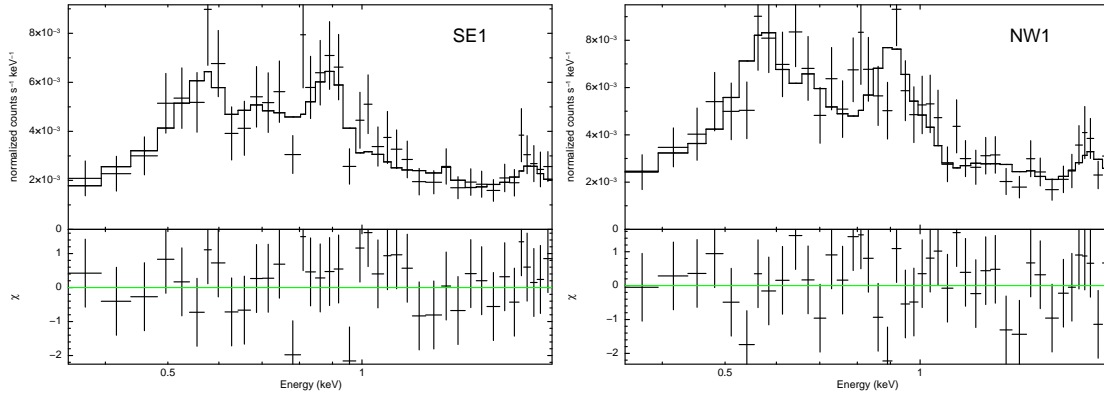


Fig. 12.— Spectra of the X-ray emission in the SE and NW sectors.

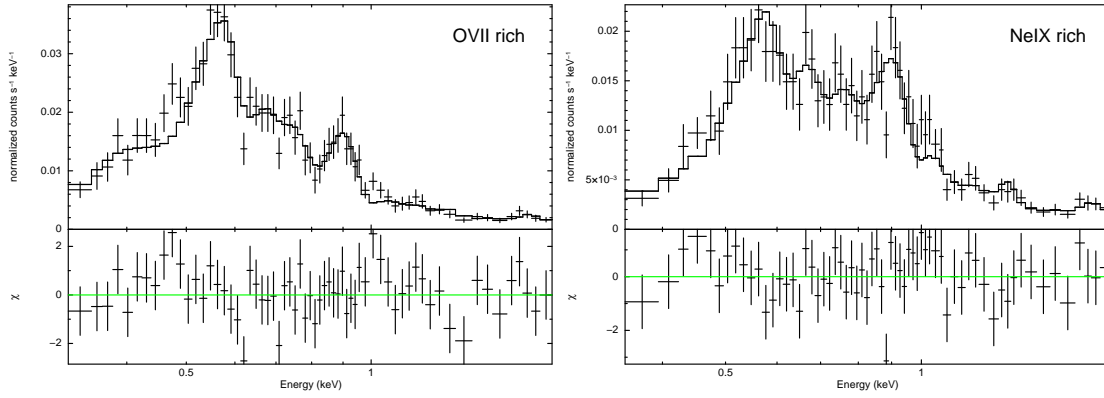


Fig. 13.— Spectra of the X-ray emission in the bicone regions that are prominent in (a) 0.3–0.7 keV emission (red in Figure 5) and (b) in 0.7–1 keV emission (green in Figure 5).

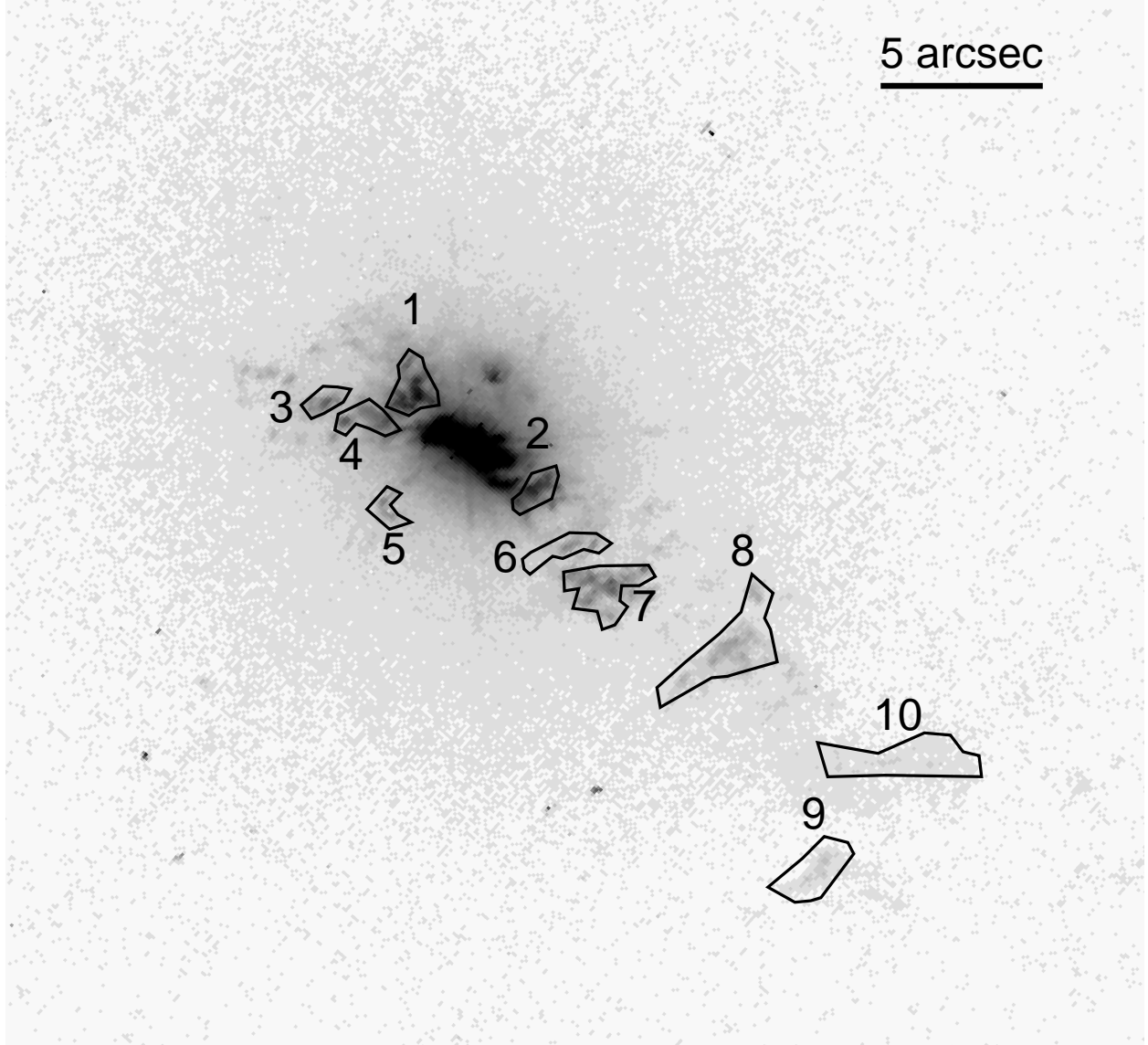


Fig. 14.— HST [OIII] clouds labeled with numbers, for which the [OIII]/soft X-ray flux ratio were derived.

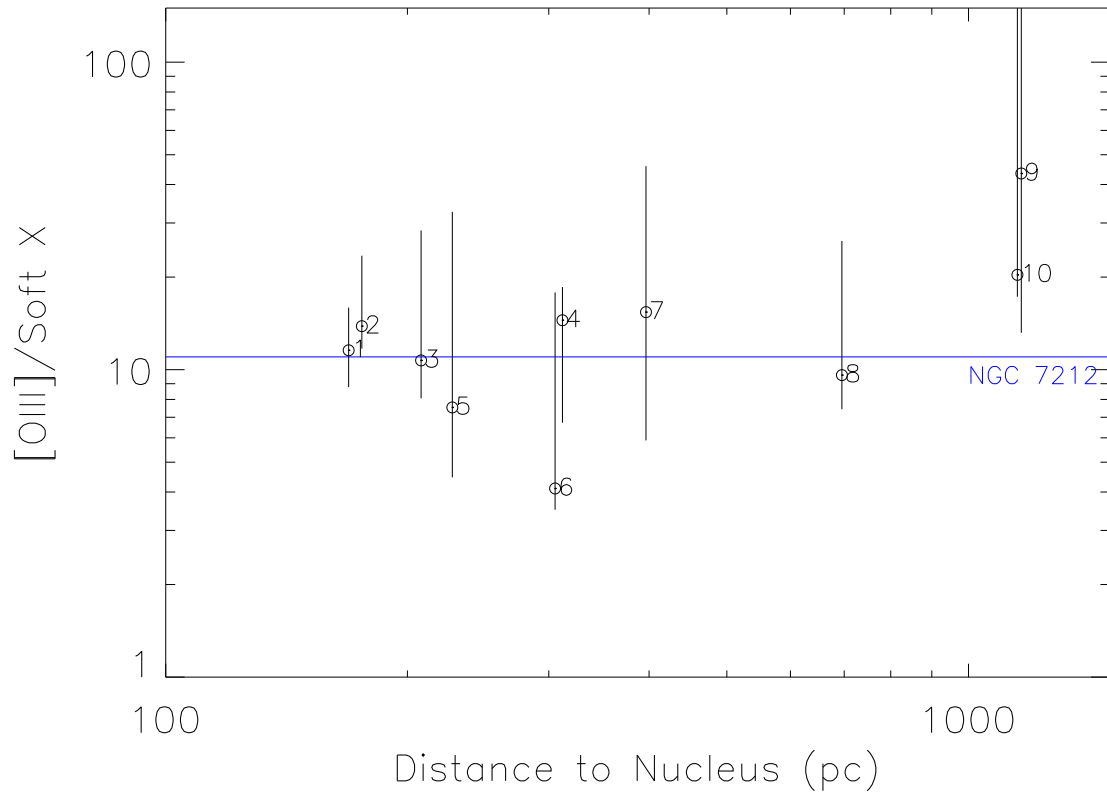


Fig. 15.— Radial dependence of the $[OIII]/\text{soft X}$ -ray flux ratio. For comparison, the ratio for the Seyfert 2 galaxy NGC 7212 (Bianchi et al. 2006) is shown.

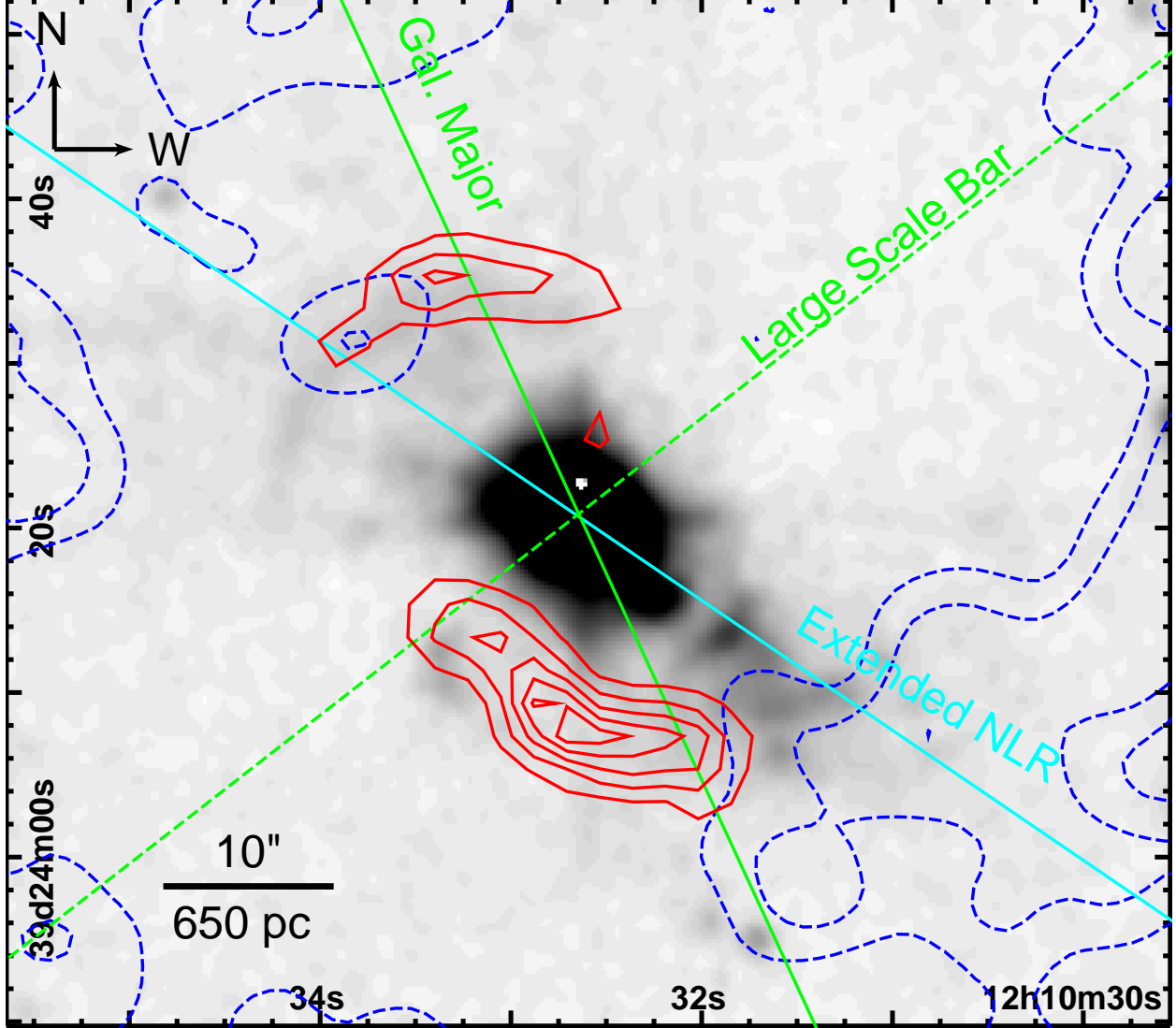


Fig. 16.— Continuum-subtracted $H\alpha$ image of the central $1' \times 1'$ of NGC 4151 obtained with the Jacobus Kapteyn Telescope (Knapen et al. 2004), which illustrates the directions of the kinematic major axis of the host galaxy (green solid line; P.A. $\sim 22^\circ$, Pedlar et al. 1992; Mundell et al. 1999), the large scale “weak fat bar” (green dotted line; P.A. $\sim 130^\circ$; Mundell & Shone 1999), and the ENLR bicone (cyan line; P.A. $\sim 65^\circ$, Evans et al. 1993). The blue and red contours show the distribution of HI (Mundell et al. 1999) and CO (Dumas et al. 2010) gas respectively.

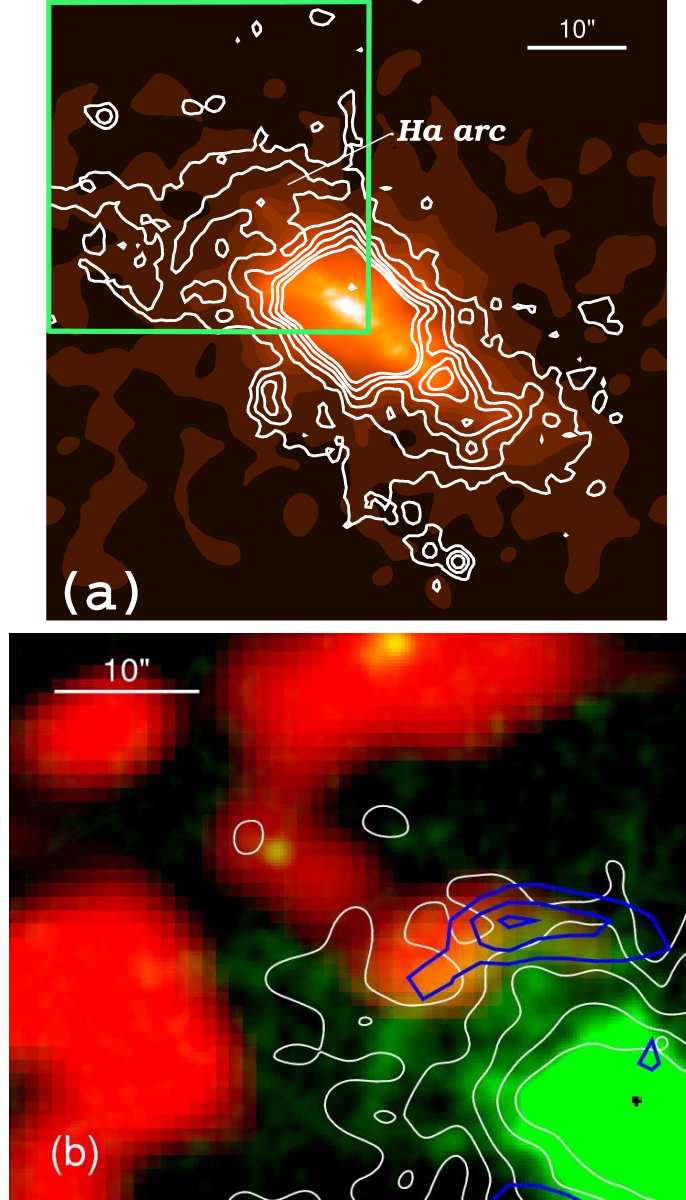


Fig. 17.— (a) Superposition of a continuum-subtracted $\text{H}\alpha$ image (contours; from Knapen et al. 2004) on the central $1' \times 1'$ of the smoothed 0.3–1 keV ACIS image. The box region is enlarged in panel *b*. (b) A composite image showing the relative distribution of HI emission in red and $\text{H}\alpha$ emission in green. Overlaid white contours are the soft X-ray emission, and blue contours the ^{12}CO emission.

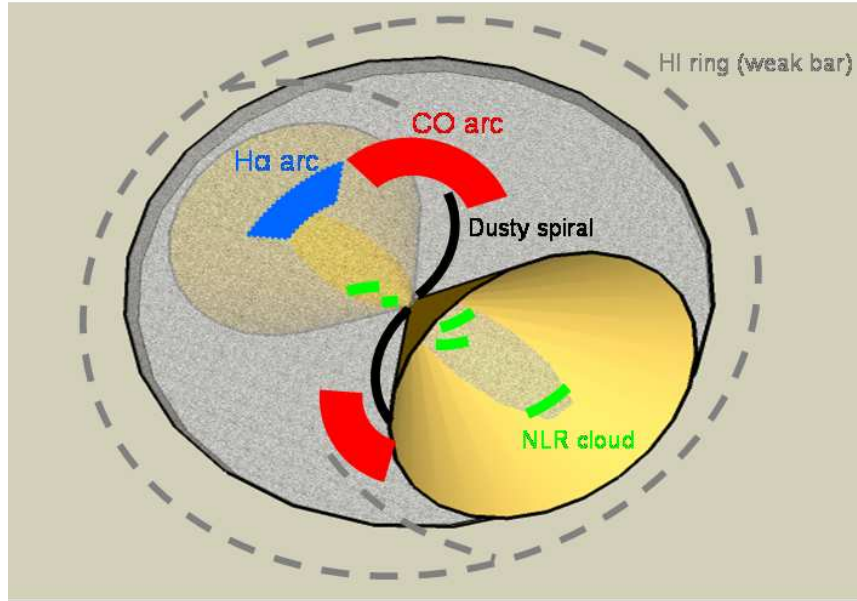
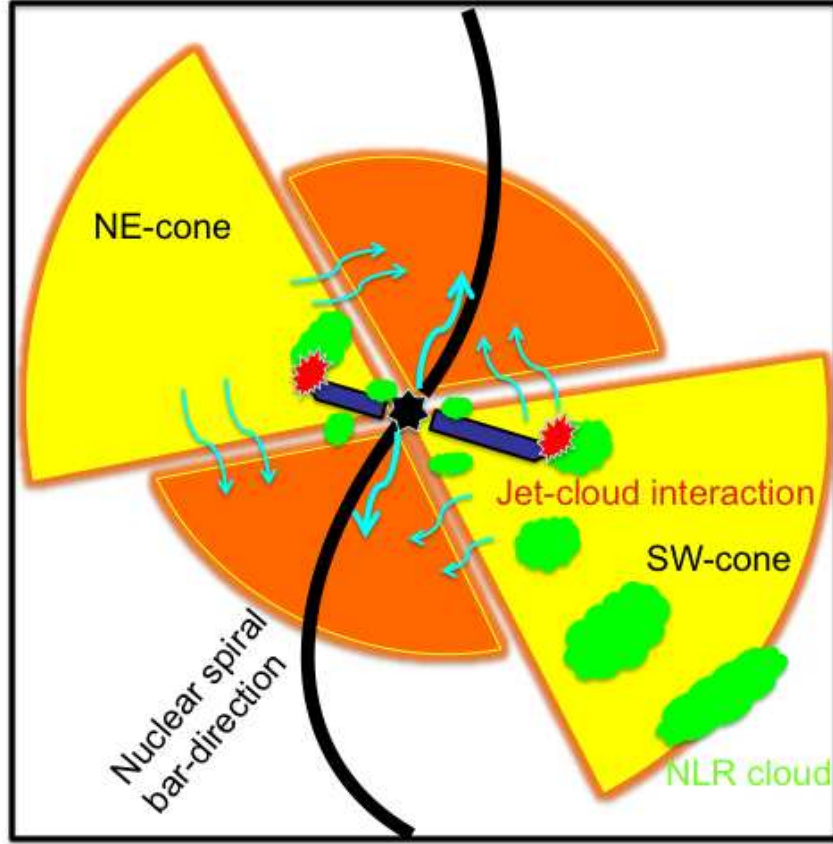


Fig. 18.— A schematic drawing of the complex circum-nuclear environment of NGC 4151. (a) The inner few hundred pc radius region; (b) The 3 kpc-across region. The features are not drawn to exact spatial scale. The cyan wiggly lines represent possible leakage/scattering of ionizing photons, whereas the orange wedges denote the lower ionization sectors perpendicular to the bi-cone (yellow wedges).

Table 1. Blended Emission Lines Identified in the Large Scale Extended X-ray Emission

ACIS Blend	HETG Lines	Observed Energy ^a [keV]	Restframe Energy [keV]	Line Flux ^b [photon cm ⁻² s ⁻¹]	ACIS/HETG Flux Ratio ^c
OVII		0.57	...	5.5×10^{-5}	13%
...	OVII f	0.5617	0.5611	3.1×10^{-4}	
...	OVII i	0.5691	0.5687	5.1×10^{-5}	
...	OVII r	0.5745	0.5740	6.8×10^{-5}	
OVIII		0.66	...	1.7×10^{-5}	13%
...	OVIII Ly α	0.6541	0.6537	1.0×10^{-4}	
...	NVII RRC	0.67	...	2.6×10^{-5}	
OVII		0.73	...	8.5×10^{-6}	12%
...	OVII RRC	0.74	...	5.2×10^{-5}	
...	OVIII Ly β	0.7749	0.7747	1.8×10^{-5}	
OVIII		0.82	...	4.4×10^{-6}	2%
...	OVIII Ly γ	0.8175	0.8171	1.1×10^{-5}	
...	OVIII RRC	0.86	...	1.1×10^{-5}	
NeIX		0.91	...	1.3×10^{-5}	21%
...	NeIX f	0.9064	0.9052	3.3×10^{-5}	
...	NeIX i	0.9172	0.9151	9.9×10^{-6}	
...	NeIX r	0.9229	0.9221	2.0×10^{-5}	
NeX		1.03	...	4.4×10^{-6}	17%
...	NeX Ly α	1.0224	1.0219	2.0×10^{-5}	
...	NeIX $1s3p - 1s^2$	1.0749	1.0738	5.9×10^{-6}	
NeX		1.20	...	1.9×10^{-6}	12%
...	NeIX RRC	1.20	...	9.3×10^{-6}	
...	NeX Ly β	1.2118	1.2110	7.4×10^{-6}	
MgXI		1.30	...	1.9×10^{-6}	9%
...	MgXI f	1.3542	1.3313	1.2×10^{-5}	
...	MgXI r	1.3525	1.3524	9.3×10^{-6}	
SiI		1.75	...	1.6×10^{-6}	9%
...	SiI K α	1.7413	1.7391	1.3×10^{-5}	
...	MgXII Ly β	1.7472	1.7450	5.3×10^{-6}	

Note. — The continuum is modeled with a bremsstrahlung (best fit $kT = 0.31$ keV) absorbed by the Galactic column $N_H = 2.1 \times 10^{20}$ cm⁻² (Murphy et al. 1993).

^aEmission line energy measured in our ACIS spectrum and in Ogle et al. (2000) HETGS spectrum.

^bline flux from the present data and in Ogle et al. (2000) HETGS spectrum.

^cRatio of the ACIS (present data) to HETGS line fluxes.

Table 2. Spectral Fits to the Extended X-ray Emission

Region	Source Counts [0.3–2 keV]	$\log N_{H,l.o.s}^a$ [$\times 10^{22} \text{ cm}^{-2}$]	$\log U_1$	$\log N_{H,1}$ [cm^{-2}]	$\log U_2$	$\log N_{H,2}$ [cm^{-2}]	Nuclear PSF ^b Counts [0.3–2 keV]	χ^2 / d.o.f.	$F_{0.5-2keV}$ $\text{erg s}^{-1} \text{ cm}^{-2} \text{ arcsec}^{-2}$
NE 1	2432	0.04 \pm 0.02	0.86	19.7	-0.22	19.7	380	63/65	6.9×10^{-15}
.... 2	1814	0.07 \pm 0.03	1.05	19.8	0.06	20.1	200	60/53	1.3×10^{-15}
.... 3	913	0.03 \pm 0.01	0.49	19.9	-1.87	23.5	140	26/29	1.7×10^{-16}
SW 1	2096	0.02	0.83	20.0	-0.38	19.4	270	60/57	1.0×10^{-14}
....2	1667	0.02	1.06	20.0	-0.42	19.8	130	58/45	2.9×10^{-15}
....3	1560	0.02	1.00	19.6	-0.50	19.6	100	54/46	7.2×10^{-16}
....4	966	0.02	0.34	19.0	-1.28	23.5	80	34/30	4.5×10^{-17}
NW	1050	0.22 \pm 0.02	1.03	19.2	-0.98	19.5	400	35/35	3.1×10^{-16}
SE	1081	0.16 \pm 0.04	1.26	20.3	-1.16	19.9	530	28/33	2.2×10^{-16}
OVII-rich	2626	0.02 \pm 0.02	0.14	20.3	-1.22	20.3	200	60/56	4.3×10^{-15}
NeIX-rich	2141	0.07 \pm 0.02	0.6	19.6	-0.21	20.4	210	50/56	4.0×10^{-15}

^aThe line-of-sight absorbing column density towards the photoionized emission. For the SW regions, the fitted $N_{H,l.o.s}$ prefers values lower than the Galactic column towards NGC 4151, and was fixed at $N_H = 2 \times 10^{20}$ (Murphy et al. 1996).

^bExpected counts from simulation of PSF scattered nuclear emission.

Table 3. Measured X-ray and [OIII] Fluxes for the Clouds

Cloud Number	Distance to Nuc. (")	Distance to Nuc. (pc)	[OIII] flux (10^{-14} ergs s $^{-1}$ cm $^{-2}$)	0.5-2 keV flux (10^{-15} ergs s $^{-1}$ cm $^{-2}$)	$F_{[OIII]}/F_{[0.5-2keV]}$
1	2.6	169	29.8 \pm 1.9	25.7 \pm 5.2	11.6
2	2.7	175	21.1 \pm 2.0	15.2 $^{+1.0}_{-5.4}$	13.8
3	3.2	208	2.6 \pm 0.4	2.4 $^{+0.3}_{-1.3}$	10.7
4	4.8	312	7.9 \pm 0.9	5.4 $^{+5.0}_{-0.7}$	14.5
5	3.5	228	1.2 \pm 0.4	1.6 $^{+0.2}_{-1.0}$	7.5
6	4.7	306	1.9 \pm 0.2	4.7 $^{+0.2}_{-3.5}$	4.1
7	6.1	397	10.2 \pm 6.0	6.6 $^{+0.5}_{-3.1}$	15.2
8	10.7	696	3.9 \pm 0.7	4.2 $^{+0.2}_{-2.5}$	9.6
9	17.9	1164	0.9 \pm 0.1	0.2 $^{+0.4}_{-0.2}$	43.4
10	17.7	1151	1.8 \pm 0.1	0.9 $^{+0.1}_{-0.8}$	20.3

Note. — The [OIII] flux is measured from F502N image.